Research Square

Preprints are preliminary reports that have not undergone peer review.
They should not be considered conclusive, used to inform clinical practice,
or referenced by the media as validated information.

MEGF10 Accelerates a Developing Niche to Improve Engrafted Progenitor Cell Retention in Dystrophic and Regenerating Skeletal Muscle

Michael Hicks
mrhicks1@uci.edu

UC Irvine https://orcid.org/0000-0001-8626-0927

Benjamin Clock
University of California, Irvine

Sebastien Colobong
University of California, Irvine

Nikitha Pavar
University of California, Irvine

Skyler Lu
University of California, Irvine

Nathaniel Addonizio
University of California-Irvine https://orcid.org/0009-0005-2375-730X

Manuel Michel
University of California, Irvine

Anita Lakatos
University of California, Irvine

Joanne Kim
University of California, Irvine

Article

Keywords:

Posted Date: April 17th, 2026

DOI: https://doi.org/10.21203/rs.3.rs-9408825/v1

License: This work is licensed under a Creative Commons Attribution 4.0 International License. Read Full License

Additional Declarations: There is **NO** Competing Interest.

MEGF10 Accelerates a Developing Niche to Improve Engrafted Progenitor Cell Retention in Dystrophic and Regenerating Skeletal Muscle

Benjamin Clock[1,2], Sebastien Colobong[1], Nikitha Pavar[1], Xinyu Lu[1], Nate Addonizio[1,2], Manuel Michel[1], Anita Lakatos[2], Joanne Kim[1], Michael Hicks[1,2,3]

Author Affiliations

1. University of California, Irvine, School of Medicine, Department of Physiology and Biophysics.

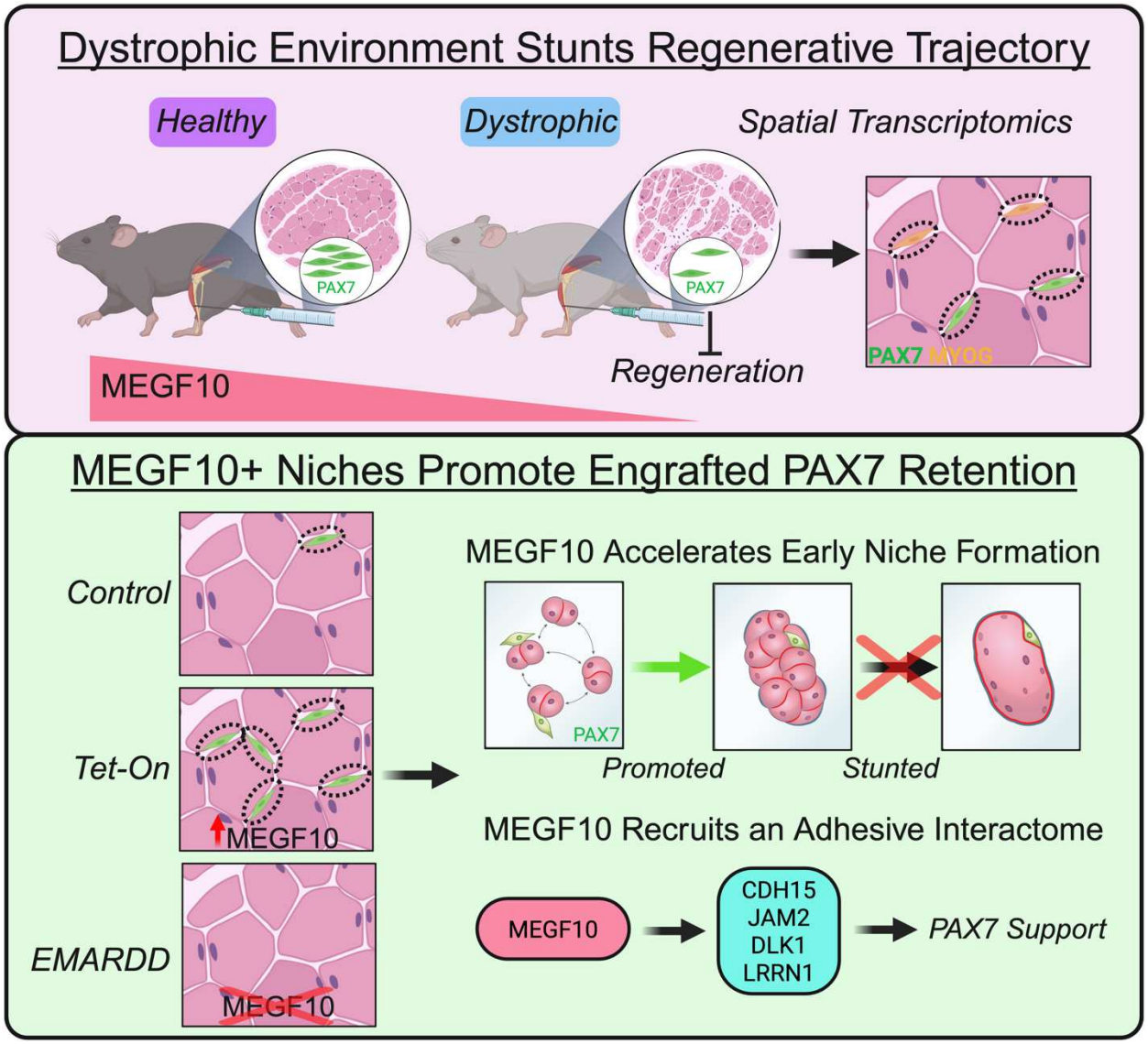
2. Sue and Bill Gross Hall, Stem Cell Research Center, University of California Irvine

3. Lead contact and corresponding author: mrhicks1@hs.uci.edu

ABSTRACT

Skeletal muscle cell therapies are limited by poor long-term engraftment, particularly in diseased muscle, where retention of a PAX7+ stem cell pool depends on formation of a supportive niche. Here, we used spatial transcriptomics to map niche development across engraftment time, healthy versus dystrophic microenvironments, and secondary injury. Engrafted myogenic cells underwent rapid early transcriptional remodeling and marked donor-cell loss, whereas regenerating myofibers acquired niche-associated programs that stabilized surviving PAX7+ cells. Dystrophic microenvironments impaired niche maturation, altered donor-cell state, and blunted regenerative adaptation after reinjury. MEGF10 emerged as an early niche-associated regulator that was transiently expressed during healthy regeneration but persisted in dystrophic muscle. Using CRISPR-engineered hPSC models, we found that MEGF10 induction during the first 10 days after transplantation more than doubled PAX7+ cell retention and donor-derived myofiber output, whereas MEGF10 loss of function, which models a severe early onset myopathy, failed to maintain engrafted PAX7+ cells. Spatial profiling of Tet-On engraftments identified a MEGF10-responsive regenerative myofiber program linked to early niche support. These findings define an early therapeutic window for improving muscle cell transplantation.

GRAPHICAL ABSTRACT



HIGHLIGHTS

- The dystrophic environment induces ECM expression in engrafted human muscle at the expense of regeneration.
- Myogenic progenitors better establish niche competence after secondary injury which is stunted in dystrophic environments.
- Engrafted muscle progenitors rapidly lose niche receptors, which is reversed by the formation of regenerative myofibers.
- Controlled dynamic expression of MEGF10 *in vivo* can improve PAX7 support and retention by stabilizing niche development.

INTRODUCTION

Skeletal muscle regeneration is essential for maintaining tissue function and quality of life but can become impaired in aging or neuromuscular diseases. Cell-based therapies offer a promising strategy to restore muscle function by repairing damaged tissue and replacing an exhausted or dysfunctional stem cell pool [1, 2]. However, efficient support of engrafted cells and retention of a stem cell pool capable of long-term regeneration remain a barrier to therapeutic development. Early myoblast transplantation studies established that, without the ability to replenish a self-renewing stem cell pool, these approaches provide only limited and short-lived benefit [3, 4]. Retention of a PAX7+ stem cell pool after engraftment depends on formation of a supportive muscle stem cell niche [5, 6], which is comprised of a basal lamina and extracellular matrix, the adjacent myofiber, and microenvironmental cues including secreted factors and cell-matrix signaling [7, 8]. How muscle stem and progenitor cells establish niches after transplantation, and how the tissue microenvironment influences this process, remain incompletely understood. Defining how transplanted human muscle cells regenerate, establish niches, and adapt to the *in vivo* environment, particularly in diseased muscle, is therefore essential for the development of effective stem cell therapies.

Human pluripotent stem cells (hPSCs) offer a potential solution for studying niche development and improving cell therapies because they can be genetically engineered with niche-associated transgenes or disease-associated modifications and subsequently differentiated into skeletal muscle progenitor cells (SMPCs) for preclinical disease modeling and at scales relevant for human therapy [9]. Directed differentiation of hPSCs to skeletal muscle generates heterogeneous cultures that support PAX7+ SMPCs for weeks to months *in vitro* [10-15]. However, hPSC-derived SMPCs are functionally immature and transcriptomically resemble early fetal muscle progenitor cells [16], which are associated with inefficient niche formation after engraftment [5] potentially due to unique cell-niche interactions that differ from adult satellite cells. Following transplantation, some teams found that only a small fraction of PAX7+ SMPCs are

retained, although those that successfully occupy niches can adopt a more mature gene-expression profile overtime resembling adult-like satellite cells [17]. Improving the ability of transplanted SMPCs to establish niches *in vivo* and persist as a quiescent stem cell pool is therefore essential for developing long-term cell therapies for patients with myopathies.

Since cell-based therapies will ultimately be deployed in diseased muscle, it is equally important to understand how pathological microenvironments influence niche formation and stem cell persistence after transplantation. Niche disruption is a common feature of many myopathies, in which diseased muscle fails to adequately support endogenous stem cells, leading to impaired self-renewal and loss of tissue homeostasis [18]. Duchenne muscular dystrophy is the most common genetic disease of muscle, results from a loss-of-function mutation in dystrophin, which results in a destabilized sarcolemma and repeated myofiber degeneration, thus forcing resident stem cells to continually rebuild their niches during chronic regeneration and ultimately contribute to stem cell exhaustion [19]. In this setting, destabilization of the extracellular matrix surrounding muscle stem cells, together with inflammatory responses and altered neighboring cell populations, further disrupts the myogenic niche that normally support stem cell function [20]. Similarly, extracellular matrix disorders such as COL6A1-associated Ullrich congenital muscular dystrophy directly impair the myogenic niche leading to poor regeneration and stem cell retention [21]. Early-onset myopathy, areflexia, respiratory distress, and dysphagia (EMARDD), caused by loss-of-function mutations in the niche receptor MEGF10, is among the most severe myopathies, with cases ranging from embryonic lethality to profound fibrosis and impaired regeneration [22, 23]. Thus, muscle diseases highlight the need for therapies that can either correct intrinsic stem cell defects or replace the diseased stem cell pool with a healthy, self-renewing one through transplantation.

Microenvironmental signals that stabilize muscle stem cells within their niche must be appropriately regulated in time and space to support self-renewal and quiescence [24]. The function of niche receptors is therefore highly dependent on both developmental timing and tissue

context, as the niche interactome evolves through regeneration, maturation, and return to quiescence to sustain the stem cell pool [7]. These microenvironmental cues include secreted signals from adjacent cell populations that activate transcriptional programs promoting niche formation, myofiber hypertrophy, and tissue remodeling [25, 26]. Niche forming cues are also provided from stem cell-myofiber or cell-matrix interactions that regulate entry into, and maintenance of, activated or quiescent states. For example, M-cadherin, Tenascin-C, and Calcitonin Receptor play important roles at the satellite cell-myofiber interface and in adhesive interactions between satellite cells and the extracellular matrix, thereby supporting early niche formation, self-renewal, and quiescence [27-31]. However, we hypothesize that because the niche changes over time, receptor expression profiles that are beneficial during early regeneration may become ineffective, or even maladaptive, if sustained at later stages, and vice versa. Defining the stage-specific functions of niche receptors during engraftment and regeneration, particularly in hPSC-derived SMPCs, therefore represents an important opportunity to advance cell-based therapies.

Recent advances in spatial transcriptomics now make it possible to resolve rare satellite cell populations in their native tissue context with increasing cellular precision [32]. We therefore applied spatial transcriptomic analysis to engrafted human skeletal muscle across time in both healthy and dystrophic mice to define supportive and antagonistic microenvironmental interactions, including those arising from unperturbed and regenerating human myofibers after SMPC transplantation into mice. These studies revealed that dystrophic muscle exerts maladaptive effects on both the transcriptional interactome and functional output of donor cell therapy. Among the factors that changed across time and disease, MEGF10 emerged as a candidate niche receptor of particular interest because of its association with early myopathic disease and its understudied mechanisms, binding partners, and cellular expression patterns in skeletal muscle. To test the temporal role of MEGF10 during engraftment, we generated tetracycline-inducible and disease-modeling loss-of-function hPSC lines and examined the effects

of modulating MEGF10 expression after transplantation. Early MEGF10 induction more than doubled the engraftment efficiency of PAX7+ cells and donor-derived myofibers. Our findings identify the first 5-10 days after transplantation as a critical therapeutic window during which manipulation of niche development may improve engraftment and regenerative outcome in muscular dystrophy.

RESULTS

Regenerative trajectory mapping after engraftment of hPSC SMPCs

Although directed differentiation from hPSCs generates cultures that support PAX7+ SMPCs *in vitro*, retention of these cells after transplantation *in vivo* remain inefficient [15]. Following directed differentiation, we FACS-enriched SMPCs, briefly expanded them, and cryopreserved them for *in vivo* transplantation studies. For engraftments, we used ROSA-DTA+/- PAX7-Cre+/- NSG mice to inducibly ablate endogenous mouse Pax7 cells and thereby reduce competition from host satellite cells [5]. Tamoxifen treatment significantly depleted host mouse Pax7+ stem cells (**Figure S1A**). We then performed spatial transcriptomic analysis on fresh-frozen xenografted muscle using the GeoMX Digital Spatial Profiler [33]. An advantage of the GeoMX platform is its ability to segment defined cell populations *in situ* using antibody-based staining, enabling selective profiling of specific myogenic populations within engrafted regions. We chose spatial transcriptomics because it retains spatial relationships between engrafted cells and surrounding muscle, permits *in situ* selection of engrafted regions, and enables capture of multinucleated myofibers without the need for FACS.

To define the *in vivo* trajectory of transplanted SMPCs, we performed spatial transcriptomics at days 1, 5, 10, and 20 after engraftment (**Figure 1A**). At each time point, we profiled myogenic regenerative progression using markers for human nuclei (Lamin AC), SMPCs (PAX7), intermediate myoblasts (MYOD1), myocytes (MYOG), and human myofibers (Spectrin)

[32]. We collected 38-47 regions of interest (ROIs) per time point using segmented single- and double-positive marker morphologies and used ROIs for statistical analysis (**Figure S1B-C**).

Before comparing transcriptional changes across time, we first confirmed dataset quality and cell-type annotation through spatial transcriptomic profiles. Spatial transcriptomic profiling detected 18,678 genes across samples, of which 11,196 remained after quality control and background filtering. Each mononuclear population ROI contained approximately 5-15 individual SMPCs or myocytes, which were pooled to generate a gene expression profile, resembling bulk RNAseq. Filtered count matrices were normalized and analyzed in DESeq2 to compare engrafted myogenic populations across time (**Table S1**) [34]. To validate cell-type identities, we grouped PAX7+ SMPCs, MYOG+ myocytes, and myofibers across all time points and examined expression of canonical markers including *PAX7, MYOD1, MYOG, MYH3*, and *MYH1* (**Figure S1D**). As expected, SMPCs expressed higher levels of *PAX7*, myocytes expressed higher *MYOD1* and *MYOG*, and myofibers expressed higher *MYH3* and *MYH1* ($p<0.05$). Despite qualitative differences of *PAX7* expression levels within SMPC ROIs, these differences did not separate into statistically distinct high- and low-expressing subgroups.

Engraftment induces rapid transcriptional remodeling across myogenic populations

To complement our spatial transcriptomic analysis, we conducted histological analysis quantifying myogenic populations across time and found a sharp decline in both PAX7+ SMPCs and MYOG+ myocytes after engraftment, paralleling a global loss of human nuclei and a progressive increase in myofibers (**Figure 1B**). This early loss plateaued after day 5, suggesting that the cells that survive the *in vitro*-to-*in vivo* transition become stabilized and are subsequently maintained through supportive interactions with regenerating myofibers. We then performed principal component analysis (PCA) on all spatial transcriptomic myogenic populations across time to gain insight on the mechanisms of transcriptional remodeling and stem cell support (**Figure 1C**). Genes uniquely expressed in each population and conserved across time further

confirmed their distinct transcriptomic identities (**Figure 1D**). In particular, engrafted SMPCs and myocytes at day 1 were clearly separated from later time points, indicating that exposure to the tissue microenvironment rapidly reshapes donor cell state. To define this global *in vivo* response, we identified genes shared across time in SMPCs and myocytes. Surprisingly, more genes were downregulated after engraftment than were induced. In total, 443 DEGs captured the global transition from *in vitro* culture to the *in vivo* environment, and gene ontology analysis showed enrichment for translation, cell adhesion, cell-matrix interactions, and migration (**Figure 1E**). Among these were *TNC* and *NOTCH3,* extracellular and transmembrane niche-associated factors implicated in establishment and stability of the muscle stem cell niche [27, 35]. These data indicate rapid transcriptional reprogramming of engrafted populations that stabilizes upon regeneration of myofiber populations, suggesting potential supportive interactions at play.

We next examined temporal transcriptional changes after engraftment to define how transplanted myogenic populations remodel muscle tissue across time and how this remodeling relates to niche formation. In SMPCs, spatial transcriptomic analysis identified more than 700 DEGs from days 1 to 5 and more than 50 DEGs from days 5 to 10. Among these, musculoskeletal growth regulator *ACVR2* declined after engraftment, whereas *LRRN1*, a transmembrane receptor involved in matrix remodeling, increased (**Figure S2A**) [8, 36]. Human myocytes underwent even broader remodeling, with more than 1,800 DEGs from days 1 to 5, more than 200 from days 5 to 10, and more than 40 from days 10 to 20. Key myogenic receptors exhibited chronological trends, with *MEGF10* and *DLL1* rapidly lost on myocytes by day 5, while MCAM increased following engraftment [8, 37, 38]. Meanwhile, factors linked to fusion and myofiber assembly like *MYOM3* increased after engraftment (**Figure S2B**) [39]. These data suggest rapid early transcriptomic shifts followed by a more stabilized transcriptomic program over time.

Distinct myofiber maturation states reveal candidate mechanisms of niche support

We identified morphological and transcriptomic heterogeneity within myofiber populations after engraftment. Smaller myofibers were closely localized to neighboring engrafted human myocytes and appeared to represent donor-derived, actively regenerating fibers composed exclusively of human cells (human only), whereas larger chimeric myofibers had fused with host mouse myofibers, as indicated by the presence of mouse Lamin A/C-negative myonuclei (chimeric; **Figure 1F**) [5]. Our previous work showed that human-only myofibers support engrafted PAX7+ cells more effectively than chimeric myofibers, although the mechanisms underlying this effect were unclear [5]. We therefore used spatial transcriptomics to examine adhesive ligands and receptors that might mediate early niche formation between regenerative myofibers and PAX7+ SMPCs. This analysis revealed a distinct niche-supportive receptor profile in regenerative human-only myofibers, including significantly elevated expression of *MEGF10* and *DLK1* (**Figure 1F**), implicating candidate mechanisms and signals that promote SMPC support and niche establishment.

PCA further confirmed that human-only and chimeric myofibers represent distinct populations with separate temporal trajectories (**Figure S2C**). Human-only myofibers displayed a persistent regenerative transcriptome marked by embryonic myofiber genes *MYH3* and *ACTC1* [5, 40], along with additional regenerative markers including *PEG10*, *MYL4*, and neuromuscular junction gene *CHRND* [41-43]. In contrast, chimeric myofibers expressed higher levels of mature, non-regenerative myofiber markers including *MYH1*, *MYH2*, *ALDOA,* and *CKM* [44]. Consistent with these distinct states, *ACTC1* expression remained relatively stable over time in human-only myofibers, whereas it progressively declined in chimeric myofibers, indicating continued maturation (**Figure S2D-E**). This distinction was further supported by increased VEGFA expression over time in chimeric myofibers, a secreted factor linked to muscle regeneration and capillary remodeling [45]. Chimeric myofibers also expressed *MYH4* which may reflect some cross-hybridization of human GeoMx probes with mouse myofiber transcripts within multinucleated myofibers [46]. These findings indicate that human-only myofibers remain in a

more immature, niche-supportive state, whereas fusion into host fibers is associated with progression toward a more mature phenotype and dampening of supportive niche receptors.

Dystrophic muscle reshapes the interactome of engrafted skeletal muscle populations and impairs regeneration after secondary injury

Understanding how engraftment evolves within a dystrophic environment is critical for developing effective cell therapies for muscular dystrophies. To define how a diseased host environment alters donor cell behavior, myofiber regeneration, and niche development, we engrafted human muscle stem cells into both wildtype C57-NSG and dystrophic mdx-D2-NSG mice, a severe model of Duchenne muscular dystrophy [47]. To eliminate competition from host satellite cells during niche formation, we further crossed both strains onto inducible Pax7 ablation transgenes [5]. We then performed spatial transcriptomic profiling 30 days after engraftment, corresponding to the completion of regeneration, to compare engrafted human SMPCs and myofibers in healthy and dystrophic muscle (**Figure 2A**). Across conditions, we captured and analyzed 26–28 ROIs containing both PAX7+ SMPCs and myofiber populations (**Figure S3A**).

Engraftment into both healthy and dystrophic muscle produced PAX7+ SMPCs and human spectrin+ regenerative myofibers. However, the dystrophic environment markedly impaired niche formation by engrafted PAX7+ SMPCs, reducing niche establishment from 77% in healthy muscle to 45% in dystrophic muscle (**Figure 2B**). PCA stratified by microenvironment and cell type revealed clear separation between healthy and dystrophic engraftments, indicating that the host tissue environment strongly influences the transcriptional state of transplanted cells (**Figure 2C-D**). PC1 primarily captured the distinction between SMPCs and myofibers, whereas PC2 reflected transcriptional differences associated with the host microenvironment (**Table S2**). To define this global microenvironmental response, we used DESeq2 to compare differential gene expression across tissue contexts and retained genes shared by both SMPCs and myofibers. This analysis identified 97 SMPC-associated DEGs in dystrophic engraftments compared with 44

in healthy engraftments, while comparison of healthy and dystrophic myogenic populations overall revealed more than 2,000 DEGs, underscoring broad divergence in both donor cell state and regenerative maturation across tissue environments.

Gene ontology analysis of genes associated with a healthy microenvironment highlighted programs related to myofiber contraction, muscle maturation, and integrin-mediated cell interactions, whereas dystrophic microenvironment-associated genes were enriched for extracellular matrix organization and cytokine-responsive pathways (**Figure 2E**). The mdx-D2 environment also induced donor-cell expression of genes linked to osteogenic and chondrogenic states, suggesting that the *in vivo* plasticity of engrafted SMPCs is altered in dystrophic muscle.

We next projected selected genes representing both shared microenvironment-responsive programs and uniquely expressed genes across cell type and tissue context (**Figure 2F-G**). Among genes enriched in dystrophic engraftments, *PAM16*, a regulator of mitochondrial protein import with reported links to immune-associated signaling was the top unbiased DEG, while *COL1A1* was the most prominent matrix-associated DEG, paralleling collagen trends in aged fibrotic settings [48, 49]. In contrast, healthy engraftments showed increased expression of *LYRM2*, which is associated with mitochondrial function, and *NCOA1*, a regulator of skeletal muscle maturation [16]. Within SMPCs, healthy tissue favored expression of the ECM-associated factor *LAMB1* and the cadherin-linked niche regulator *CTNNB1*, whereas dystrophic tissue increased expression of *NOTCH3, DLL3*, and the differentiation-associated marker *SP7* [28, 50]. Regenerative myofibers also showed marked divergence between healthy and dystrophic environments, with differences in both adhesive signaling and maturational state contributing to the more than 2,000 DEGs identified across tissue contexts. These findings demonstrate that the host microenvironment is a dominant determinant of engrafted cell state, rewiring adhesive and transcriptional programs to drive fundamentally distinct regenerative outcomes in healthy and dystrophic muscle.

Dystrophic microenvironments limit regenerative recovery after secondary injury

Given the marked differences in transcriptomic state and niche colonization by engrafted PAX7+ SMPCs in dystrophic muscle, we next tested their functional regenerative potential. Since secondary injury after initial regeneration provides a stringent measure of stem cell potency *in vivo* [51], we induced reinjury with $BaCl_2$ 30 days after SMPC engraftment in healthy and dystrophic muscle (**Figure 3A**). In both settings, secondary injury increased the frequency of PAX7+ SMPC niche formation; in mdx-D2-NSG muscle, niche establishment rose from 44% to 74% ($p<0.05$). However, healthy engraftments still supported superior niche formation compared with dystrophic engraftments (**Figure 3B**). Consistent with this, dystrophic muscle produced significantly fewer engrafted myofibers and SMPCs after secondary injury, indicating a stunted regenerative response (**Figure 3C-D**).

Spatial transcriptomic analysis further showed that the host microenvironment determined how donor cells responded to reinjury. In healthy engraftments, both SMPCs and myofibers underwent a clear transcriptomic shift after secondary injury, whereas dystrophic engraftments showed only limited change through PC analysis (**Figure 3E**). SMPCs in healthy muscle exhibited extensive transcriptional remodeling, with more than 300 genes changing with re-injury. By contrast, SMPCs in dystrophic muscle showed only ~20 total DEGs across this transition, consistent with a muted regenerative response imposed by the host environment (**Figure 3F**). Among the genes that resolved after secondary injury in healthy engraftments were the developmental niche-associated factors *MEGF10*, *TNC*, and *MCAM* [8], whereas their expression remained sustained in dystrophic engraftments (**Figure 3G**). These data indicate that dystrophic muscle not only reduces regenerative output after reinjury, but also prevents engrafted SMPCs from appropriately transitioning and maturing their niche transcriptional state.

Regenerative myofiber populations also underwent divergent responses to secondary injury in healthy and dystrophic environments. Dystrophic engraftments had reduced myofiber maturation after secondary injury, as indicated by reduced expression of *MYH1* and increased

fetal *MYH8* expression (**Figure S3B**). Notably, the adhesive ligand-receptor programs associated with niche support also differed substantially after reinjury. *MEGF10*, *LRRN1*, and *MCAM* were expressed at significantly higher levels in healthy engrafted myofibers before reinjury, whereas the early fusion regulator *NID1* is upregulated after reinjury in dystrophic engraftments [52]. These findings suggest that healthy and dystrophic microenvironments differentially regulate the adhesive and maturational programs of regenerative myofibers, with likely consequences for niche re-establishment after injury.

These transcriptomic analyses across time and disease identify a temporally regulated niche-associated program during engraftment and regeneration. Notably, MEGF10, TNC, and MCAM were most highly expressed in regenerating human-only myofibers rather than in PAX7+ SMPCs, suggesting that niche-promoting signals may arise from the myofibers themselves. In dystrophic muscle, persistence of this early regenerative program together with reduced PAX7+ cell number and impaired myofiber maturation is consistent with defective niche progression.

CRISPR-engineered hPSCs model inducible MEGF10 gain and EMARDD-associated loss of function

We hypothesized that prolonging the early niche-like state would extend the window during which newly engrafted SMPCs can establish stable niches. Since MEGF10 was consistently associated with early niche formation, and because loss of MEGF10 causes the severe and often fatal congenital myopathy EMARDD (early-onset myopathy, areflexia, respiratory distress, and dysphagia), we asked whether MEGF10 actively regulates early stages of engraftment. To test this, we generated CRISPR-engineered hPSC models for both inducible MEGF10 overexpression and disease-relevant MEGF10 loss of function.

We first generated an inducible Tet-On MEGF10 overexpression system in hPSCs. This system uses a reverse tetracycline transactivator (rtTA) that responds to doxycycline to drive transgene expression [53]. Using CRISPR-mediated homology-directed repair, we inserted

EF1A-rtTA-mTagBFP2 into the AAVS1 safe-harbor locus and TET-MEGF10-tdTomato into the hROSA26 locus [54]. Separating the two core components of the Tet-On system reduced leaky MEGF10 expression and improved HDR efficiency. Inclusion of the BFP and tdTomato reporters, each linked by self-cleaving sequences, enabled selection and FACS purification of rtTA+ and Tet-On MEGF10+ cells (**Figure 4A**).

We first validated insertion of rtTA-BFP at the AAVS1 locus by RT-PCR, which confirmed rtTA expression in the clonal knock-in hPSC line relative to parental H1 hPSCs. We then inserted the TET-MEGF10-tdTomato cassette into the hROSA26 locus and verified doxycycline-inducible tdTomato expression. Although inducible tdTomato levels declined during clonal expansion, sequential sorting of tdTomato+ cells restored a highly pure inducible population (**Figure S4A**). We next differentiated Tet-On hPSCs toward skeletal muscle and enriched SMPCs by sorting for HNK1-ERBB3+NGFR+ (H-E+N+) cells. To ensure a uniformly responsive population, we pulsed cultures overnight with doxycycline before isolating a fully inducible SMPC pool (**Figure S4B**). Controls included Tet-On H-E+N+ SMPCs without doxycycline and an rtTA control line carrying only the AAVS1 knock-in without the MEGF10 transgene. Directed differentiation yielded comparable numbers of SMPCs across all lines.

To define conditions for reliable MEGF10 induction, we performed doxycycline titration and found that 2 μM efficiently induced tdTomato expression within 24 hours (**Figure S4C**). We then confirmed myogenic potential by differentiating enriched SMPCs in N2 medium (**Figure 4B**). Tet-On and control cultures both formed abundant myosin+ myotubes and PAX7+ stem cells, with no significant difference in fusion efficiency. Upon doxycycline treatment, Tet-On MEGF10+ SMPCs and myotubes overexpressed MEGF10 at both the RNA and protein levels *in vitro*. Within 6 hours of doxycycline exposure, the Tet-On line showed a roughly 10-fold increase in *MEGF10* transcript and a 350-fold increase in *tdTomato* transcript (**Figure 4C**), whereas control lines expressed low endogenous MEGF10 and no tdTomato. At the protein level, doxycycline induced a 55% increase in MEGF10 expression in the Tet-On line. Notably, MEGF10 staining localized

primarily to myotubes in differentiation cultures. these data establish the CRISPR-engineered Tet-On MEGF10 hPSC line as a robust platform to test MEGF10 function during human myogenesis and niche formation *in vitro* and *in vivo.*

To complement this gain-of-function approach with a disease-relevant loss-of-function model, we generated and analyzed EMARDD-modeling hPSC lines alongside control and Tet-On lines. Specifically, we engineered two hPSC lines carrying pathogenic MEGF10 mutations reported in the literature in exon 2 (*Takayama* et al.,) and exon 14 (*Logan* et al.,) [22, 23] (**Figure 4D**). The *Takayama* mutation models a complete loss of MEGF10, whereas the *Logan* mutation, located within a mutational hotspot, produces a truncated protein predicted to retain reduced function. After CRISPR editing, we differentiated both lines toward skeletal muscle and enriched the SMPC population. Neither mutation altered overall SMPC yield in directed differentiation cultures (**Figure S4D**). However, when differentiated into myotubes *in vitro,* the two mutant lines showed distinct phenotypes. *Logan* SMPCs fused less efficiently than controls, whereas *Takayama* SMPCs showed increased fusion efficiency but also contained fewer PAX7+ cells, and those remaining were less proliferative (**Figure 4F**). In contrast, *Logan* cultures showed no change in PAX7+ cell density. These distinct behaviors indicate that different MEGF10 mutations exert nonuniform effects on human muscle stem cell function, consistent with the phenotypic heterogeneity observed in EMARDD.

MEGF10 overexpression shifts SMPCs toward a proliferative transcriptional state *in vitro*

To gain initial mechanistic insight into MEGF10 function *in vitro*, we performed directed differentiation followed by doxycycline induction during the final 7 days in Tet-On MEGF10 and rtTA control cultures. SMPCs were FACS-enriched using H-E+N+ tdTomato+ and immediately profiled by bulk RNA-seq (n=4-5, **Figure 5A**). PCA showed clear separation between control and Tet-On MEGF10 SMPCs (**Figure 5B**). Differential expression analysis identified 946 genes enriched in control SMPCs and 243 enriched in Tet-On MEGF10 SMPCs, including *MEGF10* itself

among the induced transcripts in Tet-On SMPCs (**Figure 5C** and **Table S3**). Gene ontology analysis indicated that control SMPCs were enriched for cell adhesion, extracellular matrix assembly, and integrin-signaling programs, whereas Tet-On MEGF10 SMPCs were enriched for proliferation-, Notch-, and migration-associated pathways (**Figure 5D**). Consistent with this, Tet-On MEGF10 SMPCs upregulated several Notch pathway genes, including *HES1*, *RBPJ,* and *HES7*, as well as early myogenic regulators such as *PAX3* and *EYA1* [55] (**Figure 5E**). They also expressed higher levels of proliferation-associated genes, including *HMMR*, *CCNB1*, and *AURKA* [56, 57]. Interestingly, *TNC*, which closely paralleled MEGF10 expression in engrafted SMPCs, was also upregulated on Tet-On SMPCs, further suggesting an interplay between these early niche-forming factors. In contrast, control SMPCs showed higher expression of adhesion- and matrix- and integrin-signaling genes such as *LAMA5* and *VTN* [58]. These data indicate that MEGF10 overexpression shifts SMPCs toward a more proliferative and activated transcriptional state, whereas control SMPCs adopt an altered adhesive interactome and gene-expression profile.

MEGF10 acts during the first 10 days after engraftment to support PAX7+ cell retention and niche incorporation *in vivo*

Since MEGF10 was enriched in early regenerative, niche-supportive myofibers during engraftment, we next asked whether prolonging this transient window could improve donor-cell retention *in vivo*. The inducible Tet-On system provided a unique opportunity to control MEGF10 expression across defined phases of regeneration and thereby determine when MEGF10 activity is most critical for engraftment. We therefore pulsed MEGF10 overexpression during early, intermediate, or late phases of engraftment in our human muscle stem cell niche model and compared these groups with control and EMARDD loss-of-function engraftments (**Figure 6A**). Robust MEGF10 expression was confirmed *in vivo* by immunostaining, validating the feasibility

of this inducible approach. Strikingly, MEGF10 was strongly expressed on regenerative human-only myofibers, but not detected in human-mouse chimeric myofibers (**Figure 6B**).

We then assessed engraftment efficacy across groups. Control engraftments yielded ~70 PAX7+ SMPCs and 200 myofibers per cross sectional area (CSA; **Figure 6D**). Early MEGF10 induction, from day 0 to day 10 after engraftment, significantly improved both donor cell retention and regenerative output, increasing engraftments to ~200 PAX7+ SMPCs and 400 myofibers per CSA. In contrast, intermediate or late MEGF10 induction did not improve engraftment over control, and induction of MEGF10 for the full engraftment period decreased engraftment efficiency with several mice showing no detectable donor cells. Complementing our gain-of-function approach, EMARDD engraftments generated myofiber numbers comparable to controls but failed to retain any PAX7+ SMPCs, indicating that MEGF10 is required for stem cell maintenance.

We then quantified niche colonization across all groups. Compared with controls, early and intermediate MEGF10 overexpression did not alter niche colonization after regeneration. However, late overexpression of MEGF10 yielded significantly more PAX7 cells outside of their niches (**Figure 6E**). These data indicate that the timing of MEGF10 expression is critical, with induction during the first 10 days after engraftment providing the strongest support for PAX7+ cell retention and productive niche incorporation.

MEGF10 signaling supports engrafted PAX7+ cells by extending early niche-forming myocyte states

To distinguish direct early effects of MEGF10 signaling from secondary consequences that emerge later during regeneration, we performed spatial transcriptomic analysis of control and Tet-On engraftments 10 days after transplantation, when regeneration is ongoing and interactions between regenerating myofibers and PAX7+ SMPCs are likely central to niche establishment (**Figure 7A**). We first quantified engraftment potential at this early time point by measuring PAX7+ SMPCs and myofibers. Tet-On engraftments contained significantly more PAX7+ SMPCs and

myofibers than control and EMARDD samples, indicating that MEGF10 promotes donor cell support during the same window in which it is overexpressed ($p<0.05$; **Figure 7B**).

Since our *in vitro* data suggested altered proliferative behavior, we next assessed PAX7+ cell proliferation *in vivo* by administering EdU during the final 24 hours before tissue harvest. At day 10, Tet-On SMPCs were less proliferative than controls, despite their greater abundance, indicating that MEGF10 alters the temporal dynamics of donor-cell proliferation during regeneration (**Figure 7C**). This result contrasted with our *in vitro* bulk RNA-seq data, which suggested a more proliferative SMPC state, and instead points to a dominant influence of the regenerative myofiber compartment and the in vivo environment on donor-cell proliferation. When we examined niche localization in these actively regenerating grafts, Tet-On engraftments showed a lower percentage of PAX7+ cells positioned within niches than controls at this stage. In parallel, EMARDD engraftments at day 10 generated myofiber numbers comparable to controls but failed to support detectable PAX7+ SMPCs, further supporting a specific requirement for MEGF10 in early stem cell retention.

We then performed spatial transcriptomic analysis on day 10 control and Tet-On engraftments, capturing 42-43 ROIs from PAX7 and myofiber populations from each treatment (**Figure S5A**). This early analysis revealed additional heterogeneity within the regenerative myofiber compartment, including a distinct early regenerative population that we classified as myocytes (**Figure S5B**). These spectin+ myocytes likely contain MYOG+ myogenic nuclei and small actively fusing bundles that are morphologically less mature than larger myofibers. Although Tet-On myocytes expressed MEGF10, expression was even higher in myofiber regions. Comparison of control myocytes and myofibers confirmed that these populations were transcriptionally distinct, with over 700 DEGs distinguishing the myogenic groups (**Table S4**).

PCA of the spatial transcriptomic data showed segregation by myogenic populations and genotype, with Tet-On and control populations clustering separately on PC2 (**Figure 7D**). In control engraftments, myocytes were transcriptionally more similar to PAX7+ cells than to

myofibers, whereas in Tet-On engraftments myocytes shifted toward a more myofiber-like state. Spatial transcriptomic analysis also validated the Tet-On system, showing significantly increased MEGF10 transcript levels across all myogenic populations *in vivo* (**Figure 7E**).

To define the broader MEGF10 response, we identified DEGs between control and Tet-On engraftments across each myogenic population. PAX7+ SMPCs differed by more than 40 genes, whereas myocytes and myofibers differed by more than 2,000 and 900 genes, respectively, indicating that the strongest transcriptional effects of MEGF10 occurred in the regenerative myocyte and myofiber compartments. Across Tet-On myocytes and myofibers, 299 DEGs were shared, and gene ontology analysis showed enrichment for translation, muscle contraction, and TOR signaling (**Figure 7F**). Several genes linked to niche development, early fusion, and regenerative myogenesis, including niche receptors *CDH15, JAM2, DLK1*, and *LRRN1*, were significantly upregulated in Tet-On regenerative engraftments, shedding light on the mechanism of action of the MEGF10 signaling cascade (**Figure 7G**).

Finally, we examined how MEGF10 signaling affected myofiber development within regeneration. Tet-On MEGF10+ myocytes displayed a more regenerative profile, with higher expression of fusion-associated *MYOM2*, the developmental myosin *MYH8* (**Figure S5C-D**). In contrast, control myofibers appeared more developmentally advanced and less regenerative, with higher expression of the mature myofiber marker *MYH1* and *FHL1*, whereas Tet-On myofibers retained higher expression of immature markers such as *ACTC1*. Together, these data indicate that MEGF10 prolongs an early regenerative myocyte state and delays full myofiber maturation, thereby extending a developmental window that is associated with improved PAX7+ cell support during engraftment.

DISCUSSION

Our study found successful human muscle progenitor cell engraftment depends on a transient regenerative niche that forms during the initial phase of myofiber repair. By integrating

spatial transcriptomic profiling across time, regenerative states, and healthy versus dystrophic host environments from multiple independent datasets, we resolved how the myogenic niche emerges, progresses, and fails. Our analyses show dystrophic muscle alters engrafted SMPC transcriptional programs, disrupts niche progression after reinjury, and inhibits many regenerating myofibers from maturing. MEGF10 emerged as a functional regulator of this early window, and stage-specific MEGF10 induction in SMPCs improved PAX7 retention and regenerative output, whereas EMARDD-associated MEGF10 loss-of-function failed to retain any engrafted stem cells. Our findings demonstrate that the early developing niche is a critical determinant of engraftment success, establishes the dystrophic microenvironment as a barrier to myogenic niche progression, and identifies MEGF10-dependent signaling as a potential therapeutic target to improve muscle stem cell transplantation.

For cell- and gene-based therapies to be successful, it is essential to understand how diseased host environments alter the behavior, persistence, and regenerative capacity of muscle stem and progenitor cells [59, 60]. Through spatial transcriptomics, we found that healthy donor SMPCs engrafted into dystrophic muscle adopt a transcriptional state marked by persistent failure to resolve gene programs that normally extinguish *in vivo*, accompanied by a shift toward osteogenic and chondrogenic differentiation. These SMPCs remain abnormally activated and showed evidence of altered mitochondrial stress and adaptation within the dystrophic microenvironment. These state changes were accompanied by reduced PAX7+ niche colonization and a diminished capacity to repopulate the niche after secondary injury, indicating that dystrophic muscle compromises both initial niche establishment and long-term regenerative competence. Notably, engrafted SMPCs upregulated extracellular matrix genes, raising the possibility that healthy cells can also contribute to maladaptive remodeling in a disease context. These findings corroborate prior studies which show healthy recipient muscle supports more robust engraftment than dystrophic muscle [61], and wild-type ECM is more permissive for progenitor remodeling and differentiation than dystrophic mdx ECM [62]. More broadly, they

underscore the suggested requirement for combinatorial strategies that improve both donor-cell fitness and the host microenvironment in dystrophic muscle.

Upon engraftment, hPSC-derived myogenic progenitors undergo developmental maturation *in vivo*, which in turn gives rise to increased regenerative potency [17]. Although previous bulk RNAseq studies of engrafted muscle provided important insight into *in vivo* maturation, spatial transcriptomics preserves tissue architecture and enables engrafted heterogenous myofiber populations to be analyzed *in situ* without disrupting the multinucleated fibers [63]. By resolving all populations directly within engrafted muscle, our analysis substantially advances prior work by uncovering previously unrecognized heterogeneity among engrafted hPSC-derived myofibers, enabling us to better define how distinct myofiber populations contribute to SMPC niche development and support. We found that transplanted myocytes begin expressing regenerative myogenic genes within 1 day of engraftment and can form robust myofibers by day 5. This rapid regenerative progression was accompanied by a global transcriptional response significantly enriched in engrafted myofibers rather than in SMPCs, suggesting that niche development is closely linked to myofiber regeneration and that these factors may help stabilize and retain the PAX7+ SMPC pool. Human-only myofibers appear to represent an early niche-supportive state that is particularly effective at maintaining engrafted PAX7+ SMPCs, likely because they upregulate key niche receptors and are most closely associated with PAX7+ cells histologically [5], yet they transition more slowly toward a mature myofiber state. One possible explanation is that these donor-derived fibers remain incompletely integrated within the larger host muscle, whereas fusion with host mouse myofibers to form chimeric fibers may provide structural or signaling cues that promote further maturation. Secondary injury appeared to be the most effective condition for improving this integration and advancing niche progression. Functionally, reinjury also enhanced the ability of engrafted SMPCs to occupy the stem cell niche, suggesting that regenerative remodeling of the host environment promotes both myofiber integration and productive niche maturation.

MEGF10 appears to act during a defined early phase of regeneration, promoting establishment and extension of the primary engrafted myogenic niche rather than maturing into a later secondary niche. Although early donor-cell loss is widely recognized as a major barrier to skeletal muscle transplantation, relatively few studies have directly analyzed engraftment during the first several days after transplantation [64], with most work focusing on outcomes measured weeks later. In our model, MEGF10 overexpression during the first 10 days accelerated differentiation and early myofiber commitment, thereby reinforcing retention of the PAX7+ SMPC pool, coincident with the period when the regenerating host-muscle environment directs stem-cell fate decisions and promotes incorporation into the emerging niche [65]. Consistent with this model, the decline in SMPC number between days 1 and 5 after engraftment paralleled reduced global MEGF10 expression, supporting the existence of a limited window for donor-cell capture. Importantly, when MEGF10 is either missing or expressed at a later regenerative stage, engraftment dynamics and PAX7 SMPC retention are significantly worsened. However, continued induction beyond day 10 also impaired further maturation, indicating that prolonged maintenance of this immature niche becomes counterproductive. As the niche, and likely the associated stem cell state, matures, it may become less supportive of initial donor-cell adhesion and incorporation and instead more supportive of a functional, quiescent state.

The physiological importance of MEGF10 in skeletal muscle is underscored by EMARDD, a severe early-onset myopathy caused by loss-of-function mutations in MEGF10 [22]. Multiple EMARDD-associated MEGF10 mutations have been described, and the distinct behaviors of the *Takayama* and *Logan* disease-modeling EMARDD variant lines parallel the variability in affected patients ranging from death *in utero* to survival into early adulthood. Our data support the idea that different MEGF10 mutations exert nonuniform effects on human myofiber and muscle stem cell function. Despite this clinical significance, MEGF10 and its precise role in skeletal muscle homeostasis remains relatively understudied. In developing mouse skeletal muscle, MEGF10 is expressed at the interface between PAX3+ muscle progenitors and developing myofibers,

suggesting a role in embryonic niche colonization, although it remains unclear which cell type, or whether both, may be its principal source [8]. After *in vivo* engraftment of primary human fetal muscle progenitors, MEGF10 is significantly upregulated in repopulating PAX7+ SMPCs after secondary injury [5], although its relevant binding partners and interactome in skeletal muscle remain incompletely defined. In the human brain, MEGF10 functions in astrocyte-mediated debris clearance by binding the C1q receptor and triggering phagocytosis, which is consistent with a broader role in cell-cell interactions and adhesion [66].

We therefore sought to identify downstream signaling partners of MEGF10 that may contribute to the formation of a permissive niche by engrafted myogenic cells. *In vitro* RNA-seq of Tet-On MEGF10 SMPCs provided a useful baseline, revealing increased proliferation and Notch signaling. However, spatial transcriptomic analysis *in vivo* uncovered a markedly different gene-expression profile, suggesting that transcriptional programs associated with MEGF10 induction are highly dependent on the regenerative environment encountered after transplantation. This distinction is consistent with recent comparative studies in other tissues showing that even advanced *in vitro* models remain transcriptionally distinct from their *in vivo* counterparts [67]. Early MEGF10 induction *in vivo* was accompanied by increased expression of *DLK1, JAM2, CDH15*, and *LRRN1* in regenerating myofibers, identifying these genes as candidate niche associated factors. We did not identify prior evidence for a direct DLK1-LRRN1 signaling relationship, but both genes have been associated with early somite, developmental, and regenerative myogenic states, making them plausible components of a broader immature niche-supportive program [68].

Although current technologies have limitations in the ability to fully resolve the cellular and transcriptomic complexity of engrafted muscle, GeoMX-based high-plex spatial profiling provides one of the most informative approaches currently available for studying donor-cell state and niche development *in situ.* One key strength of this platform is that it preserves spatial integrity and resolution that would be lost with tissue dissociation, enabling unbiased transcriptomic analysis

of engrafted cells within their regenerative context. At the same time, it has important limitations, including segmentation overlap and incomplete resolution of true cellular heterogeneity. Since SMPCs and regenerating myofibers lie directly adjacent to one another, low levels of myofiber transcripts were detected within SMPC regions. We addressed imperfect segmentation by comparing significant genes across populations and excluding likely contaminating genes in SMPC-focused analyses (Extended Methods). In addition, because each region captures small groups of 5-15 SMPCs or myocytes and generates bulk-like expression profiles, this approach cannot fully resolve heterogeneity within engrafted populations. This limitation is particularly relevant given that spatial transcriptomic analysis as early as one day after engraftment revealed abundant myoblast-like populations, underscoring the need to improve SMPC expansion and enrichment strategies to better preserve PAX7+ cells after sorting. It remains unclear whether engrafted population heterogeneity may itself contribute to early niche formation and donor-cell retention. Finally, because our analyses relied on human-specific probes, and the extent to which the recipient mouse microenvironment, particularly in dystrophic and injured settings, contributes maladaptive signals that shape donor-cell behavior has yet to be defined.

In summary, our findings have important clinical implications and point to new avenues for improving cell-based therapies. Our data support a model in which human muscle stem cell engraftment is determined not only by donor-cell intrinsic properties, but also by a transient niche established within the first days of cell transplantation. The dystrophic microenvironment disrupts the progression of this niche, limiting both stem cell retention and regenerative recovery, whereas stage specific MEGF10 signaling prolongs an early permissive state that improves engraftment efficiency. Ongoing work will determine whether sustained MEGF10 overexpression, or more clinically tractable approaches to modulate MEGF10 signaling, can help overcome the barriers imposed by the dystrophic microenvironment and improve therapeutic regeneration in muscular dystrophy. These findings provide a basis for understanding why donor-cell loss is so pronounced after transplantation and suggest that effective cell therapies for muscular dystrophies may

require not only improved donor cells, but also strategies to recreate or extend the early niche environment that supports their incorporation.

AUTHOR CONTRIBUTIONS

BC and MH conceptualized, and designed experiments included in this study. BC, SC, NP, XL, NA, MM, JK, and MH contributed to the research foundations and analysis.

ACKNOWLEDGEMENTS

Additional thanks to Van Anh Nguyen, Shreya Pavani, Angela Li, Shanice Benson, Amanda Tedesco, Olga Jaime, and Kathy Bazan in the Hicks' Lab for research advice. Thank you to Pauline Nguyen and Vanessa Scarfone from the UCI Flow Core, Melanie Oakes, Christina Lin, Ivan Chang, and Quy Nguyen from the UCI GHTF, and Basir Syed and Aftab Ahmed from the Chapman School of Pharmacy Core. Our funding sources include the NIH R01, NIH MAXIMUS T32, MDA award, KL2 award.

FIGURE LEGENDS

Figure 1: Mapping the Regenerative Trajectory of Engrafted Human hPSC SMPCs using Spatial Transcriptomic Analysis.

A. Visual schematic of the experimental workflow for Figure 1. Engraftment of SMPCs into tibialis anterior and tissue harvesting at days 1, 5, 10, and 20. GeoMX DSP segmentation strategy shown (right) based on antibody staining for myogenic markers of interest. **B.** Immunostaining imaging of myogenic populations across time, human lamin AC (grey), PAX7 (green), MYOD1 (yellow), MYOG (purple), and dystrophin (red; right). Quantifications of myogenic populations across time; PAX7+ SMPCs, MYOG+ myocytes, Dystrophin+ myofibers, and Lamin AC+ human nuclei per cross-sectional area. One-way ANOVA statistical analysis were applied. **C.** PCA projection of spatial transcriptomic data collected from engraftment trajectory analysis. **D.** Heatmap projection

of the gene expression profile of population unique myogenic identifiers. **E.** Heatmap projection of the global response to *in vivo* microenvironment across SMPCs and myocytes after engraftment (left). Gene ontology analysis of global response genes analyzed through DAVID Gene Ontology (Statistical analysis; fisher's exact test and Benjamini-Hochberg multiple testing correction). Gene number shown next to each bar. **F.** Images from the GeoMX DSP of Human-only and Chimeric myofiber regions (left). Arrows point to LaminAC- myonuclei in chimeric myofibers. Heatmap projection of significantly upregulated muscle stem cell niche receptors on Human-only myofibers (center). Violin plots of normalized gene expression values of MEGF10 and DLK1 (right). P values included in this figure: $*p<0.05$, $**p<0.01$, $***p<0.001$, $****p<0.0001$.

Figure 2: Engrafted Human SMPC Regeneration is Determined by the Microenvironment

A. Visual schematic of experimental layout for Figure 2: engraftment into healthy and dystrophic microenvironments. **B.** Immunostaining of engrafted human skeletal muscle in healthy and dystrophic microenvironments (left). Green arrows point to PAX7 cells inside niches, while red arrows point to those outside niches. Niche colonization quantified across samples, applying a t-test for statistical analysis (right). **C.** Engrafted images from the GeoMX DSP showing the process of ROI segmentation of PAX7 cells and myofibers. Scale bars are 500μM. **D.** PCA projection of spatial transcriptomic data collected from healthy and dystrophic engraftments. **E.** DAVID Gene ontology analysis of myofiber DEGs in healthy vs dystrophic engraftments. The dotted line indicates p-value cutoff of 0.05. **F**. Heatmap projection significant hits across cell type and microenvironment. **G**. Select DEGs projected via Violin plot; PAM16, COL1A1, LYRM2, and NCOA1. P values included in this figure: $*p<0.05$, $**p<0.01$, $***p<0.001$, $****p<0.0001$.

Figure 3: Dystrophic *in vivo* environment stunts secondary injury in engrafted human muscle stem cell models.

A. Visual schematic of experimental layout for Figure 3. Pre-secondary injury (Pre) samples are collected 30 days after engraftment. Post-secondary injury (Post) samples are administered a secondary injury event 30 days after engraftment and collected after another 30 days. **B.**

Immunostaining of engrafted human skeletal muscle in healthy and dystrophic microenvironments (left). Green arrows point to PAX7 cells inside niches, while red arrows point to those outside niches. Niche colonization quantified across samples, applying a one-way ANOVA for statistical analysis (right). **C.** Engrafted images from the GeoMX DSP showing the process of ROI segmentation of PAX7 cells and myofibers. Scale bars are 500μM. **D.** Quantifications of engrafted human PAX7+ SMPCs (left) and spectrin+ myofibers (right) per cross sectional area. T-test applied for statistics. **E.** PCA projection of spatial transcriptomic data from healthy and dystrophic SMPC engraftments before and after secondary injury. **F.** Heatmap projection of significant DEGs in PAX7+ SMPCs across microenvironment and secondary injury (top). Heatmap projection of significant DEGs in myofibers across microenvironment and secondary injury (bottom). Genes associated with niche formation and myofiber maturation are color labeled. **G.** MEGF10 normalized gene expression projection via Violin plot in SMPCs (left) and myofibers (right) across microenvironment and secondary injury. **H**. Immunofluorescence image (MEGF10, PAX7, LAC/Spectrin) of healthy engraftment pre-secondary injury. Scale bar = 50μM. P values included in this figure: $*p<0.05$, $**p<0.01$, $***p<0.001$, $****p<0.0001$.

Figure 4: CRISPR HDR Mediated Generation of a MEGF10 Inducible Overexpression Skeletal Muscle Progenitor Line

A. Schematic of the first homology directed repair guided insertion at the AAVS1 locus (left). PCR verification of correct insertion with primer location annotated by purple arrows, including a wildtype negative control, parental positive control, and clonal knock-in line (left to right). Real time PCR of rtTA transcripts comparing wildtype hPSC to insertion line. Schematic of the second homology directed repair guided insertion at the hROSA26 locus (right). PCR verification of the correct insertion with primer location annotated by purple arrows, including a wildtype negative control, plasmid positive control, and clonal knock-in line before and after puromycin selection. FACS plots of this TET-on knock-in hPSC line with and without treatment of doxycycline, y-Axis

= tdTomato. **B.** Schematic detailing all described EMARDD pathological variants. The MEGF10 coding region taken from UCSC Genome Browser mapped with all known disease variants and their respective mutations (top). Selected Takayama and Logan EMARDD mutations validated through sanger sequencing of SMPCs following directed differentiation (bottom). **C.** Differentiation of FACS enriched TET-on SMPCs to myotubes using serum free N2 media *in vitro*. Immunostaining for Myosin (red), PAX7 (green), DAPI (blue). 10X image scale bar = 200μM (left). Inset is 20X image scale bar = 50μM. Fusion assay (myonuclei / total nuclei) quantified (right), statistics applied with T-test. **D.** Real Time PCR of five-day myotube differentiation cultures comparing treatment of doxycycline for the final 6hours, 1 day, 3 days and 5 days of culture. MEGF10 transcripts (left) and tdTomato transcripts (right) measured across timepoints. **E.** Immunostaining of myotube differentiation for MEGF10 (red), PAX7 (green), Myosin (grey), DAPI (blue). Images taken at 20X, scale bar = X. Quantification of MEGF10 staining (right). **F.** Differentiation of FACS enriched EMARDD SMPCs to myotubes using serum free N2 media *in vitro* (top). Quantifications for fusion assay (myonuclei / total nuclei), PAX7 density (PAX7+ nuclei / total nuclei), and PAX7 proliferation (PAX7+Ki67- nuclei / PAX7+ nuclei) shown (bottom). T-test applied for statistics. P values included in this figure: $*p<0.05$, $**p<0.01$, $***p<0.001$, $****p<0.0001$.

Figure 5: MEGF10 Regulates SMPC Interactions via the Notch Signaling Pathway

A. Visual schematic of the experimental layout for Figure 5. Tet-On cultures were administered 2μM doxycycline for the final 7 days of differentiation. **B.** PCA projection of RNAseq datasets using DESeq2 analysis. **C.** Volcano plot projection of Control and Tet-On DEGs – adjusted p value cutoff < 0.05. Selected significant DEGs are highlighted and labeled. **D.** DAVID Gene Ontology Analysis of Control and Tet-On DEGs. P value cutoff of 0.05 is indicated by the vertical dotted lines. **E.** Heatmap projection of normalized gene expression for select DEGs of interest across Control and Tet-On samples. Genes associated with Adhesion, Mitosis, and Muscle Stem

cell development are color labeled. P values included in this figure: ∗p<0.05, ∗∗p<0.01, ∗∗∗p<0.001, ∗∗∗∗p<0.0001.

Figure 6: Early MEGF10 Overexpression on Engrafted Human SMPCs Supports PAX7 Support and Improved Regeneration

A. Visual schematic of experimental workflow for Figure 6. Tet-On SMPCs not treated with doxycycline were used as Control. **B.** Engrafted Control and Tet-On samples immunostained with MEGF10, PAX7, lamin AC, and spectrin. Arrows point to PAX7 cells that are interfacing with MEGF10+ myofibers. **C.** Engrafted samples immunostained with PAX7, laminin, lamin AC, and spectrin across Control (top), Tet-On D0-10 (middle), and EMARDD (bottom). Scale bars are 200μM. Inset scale bars are 50μM. **D.** Quantifications per cross-sectional area of human Spectrin+ myofibers (left) and PAX7 cells (right). One-way ANOVA statistical test applied. **E.** PAX7 niche localization assay across groups. PAX7+ nuclei were quantified as either within basal lamina (in niche) or outside it (out niche; left). One-way ANOVA statistical test applied. Representative immunofluorescent images of each group, scale bars = 20μM (right). Green arrows point to PAX7 cells in niches, red arrows point to PAX7 cells outside niches. P values included in this figure: ∗p<0.05, ∗∗p<0.01, ∗∗∗p<0.001, ∗∗∗∗p<0.0001.

Figure 7: MEGF10 Signaling Pathway Triggers Niche Forming Factors and Accelerates Early Myofiber Regeneration

A. Visual schematic of the experimental procedure for Figure 7 (top). Tet-On samples administered doxycycline to pulse MEGF10 overexpression Days 0-10. **B**. GeoMX DSP platform scanned images of spatial transcriptomic samples of Control and Tet-On engraftments at day 10; LaminAC, Spectrin, PAX7, and MEGF10 (left). Quantifications of human myofibers (center) and PAX7 cells (right) per cross sectional area of engraftment in Control, Tet-On, and EMARDD samples, one-way ANOVA statistical test applied. **C.** EDU proliferation assay and Niche localization assay of engrafted human PAX7 cells in Control and Tet-On. Immunofluorescence

images of engraftments stained with EDU, PAX7, LaminAc, Spectrin (top), and Laminin, PAX7, LaminAc, Spectrin (middle). Green arrows point to PAX7 cells that are EDU+ (top), or inside niches (bottom). Red arrows point to PAX7 cells that are EDU- (top), or outside niches (bottom). Scale bars are 20 and 50μM respectively. Quantifications of PAX7+ EDU+/- nuclei (bottom left) and PAX7+ nuclei within/outside basal lamina (bottom right). T-test statistical test applied. **D**. PCA projection of spatial transcriptomic data. Principal component analysis was performed on normalized gene expression values across all genes, and the top 2 PCs were used to project these datasets. **E**. Violin plot of normalized gene expression counts for MEGF10 transcripts across samples. **F**. Venn diagram showing the DEGs upregulated in Tet-On myofibers and myocytes (top). 299 genes are shared between these Tet-On myogenic populations, which were input into DAVID Gene Ontology analysis for systematic categorization and association of genes (bottom). The dotted line corresponds to a p-value of 0.05, and gene numbers are labeled next to their respective bar on the graph. **G**. Heatmap projection of normalized gene expression values of global Tet-On DEGs shared across myogenic populations (top). DEGs are categorized into Niche forming / Adhesive, fusion, and immature myofiber development associated hits. Violin plots of normalized gene counts for global Tet-On DEGs. P values included in this figure: $*p < 0.05$, $**p < 0.01$, $***p < 0.001$, $****p < 0.0001$.

Figure S1: Assessment and collection of engrafted myogenic populations through spatial transcriptomic approaches.

A. Number of PAX7 cells per 175mm^2 in immunostained images of PAX7-CRE ROSA-DTA NSG mice after treatment with tamoxifen for 7 days compared to a non-treated control. Arrows point to Pax7+ nuclei. T-test statistical analysis applied. **B.** Table of all engrafted regions of interest of myogenic populations across time collected through spatial transcriptomics analysis for Figure 1, S1, and S2. **C.** GeoMX DSP platform images of immunofluorescent spatial transcriptomic samples used for ROI collection. ROIs are outlined in white boundaries in the segmentation

column and labeled according to their collected myogenic population. Scale bars are 500μM. **D.** Normalized gene expression values of myogenic cell identity genes: PAX7, MYOD1, MYOG, MYH3, and MYH1. All samples across time of the same myogenic identify are grouped together. P values included in this figure: ∗p < 0.05, ∗∗p < 0.01, ∗∗∗p < 0.001, ∗∗∗∗p < 0.0001.

Figure S2: Mapping the Regenerative Trajectory of Engrafted Human hPSC SMPCs using Spatial Transcriptomic Analysis.

A. Heatmap projection significant hits across time in SMPCs (left). Violin plots of normalized gene expression values of NOTCH3, LRRN1, ACVR1, and CDK6 (right). **B.** Heatmap projection significant hits across time in myocytes (left). Violin plots of normalized gene expression values of MEGF10, MYOM3, DLL1, and MCAM (right). **C.** PCA projection of Human-only and Chimeric myofibers across time (left). Volcano plot projection of upregulated hits in human-only vs chimeric myofibers (right). Y-axis threshold is based on padj = 0.05. **D.** Heatmap projection significant hits across time in human-only myofibers (left). Violin plots of normalized gene expression values of THBS4 and MYH4 (right). **E.** Heatmap projection significant hits across time in chimeric myofibers (left). Violin plots of normalized gene expression values of ACTC1 and VEGFA (right). P values included in this figure: ∗p < 0.05, ∗∗p < 0.01, ∗∗∗p < 0.001, ∗∗∗∗p < 0.0001.

Figure S3: Engrafted Human SMPC Regeneration and Support is Determined by the Microenvironment.

A. Table of all engrafted regions of interest collected through spatial transcriptomics analysis for Figure 2,3, and S3. **B.** Violin plot projection of normalized gene expression values of genes associated with myofiber development and maturation (MYH3, MYH8, MYH1), stem cell niche formation and adhesion (MCAM, LRRN1, NID1), extracellular matrix (TNC, COL1A1, FN1), and secreted signaling (HGF, IGF2, ANXA2). P values included in this figure: ∗p < 0.05, ∗∗p < 0.01, ∗∗∗p < 0.001, ∗∗∗∗p < 0.0001.

Figure S4: CRISPR engineering Tet-On MEGF10 overexpression and EMARDD disease modeling lines.

A. Schematic of treating TET-on hPSCs with doxycycline to activate the tdTomato reporter (top). Immunostaining of doxycycline-treated TET-on hPSCs with dsRED (red), phalloidin (green), DAPI (blue). 10X images, scale bar = 150μM. **B**. Flow cytometry analysis of doxycycline treated Tet-On SMPCs. Representative plots for non-treated control and 2μg/mL (left) and quantifications for the percentage of tdT positivity (left). One-way ANOVA statistical test applied. **C**. FACS enrichment of TET-on SMPCs following directed differentiation. HNK1 exclusion, NGFR FMO, ERBB3 FMO, ERBB3+NGFR+ double positive gating, BFP+ selection, and tdTomato gating for TET-on SMPCs +/- doxycycline treatment (left to right). Quantifications of percentage E+N+H- SMPCs collected through flow sorting across samples (right). **D**. FACS enrichment of EMARDD disease modeling SMPCs following directed differentiation, showing the ERBB3+NGFR+ gating strategy (left) and the quantification of the SMPC percentage of total viable cells (right). P values included in this figure: $*p < 0.05$, $**p < 0.01$, $***p < 0.001$, $****p < 0.0001$.

Figure S5: Early MEGF10 Overexpression on Engrafted Human SMPCs Supports PAX7 Support and Improved Regeneration

A. Table of all engrafted regions of interest collected through spatial transcriptomics analysis for Figure 7 and S5. **B**. GeoMX DSP platform scanned images of myocytes and myofibers in Control and Tet-On spatial transcriptomic samples, stained for lamin AC, spectrin, PAX7, and MEGF10 (left). The dotted circles highlight regions of regenerative myofibers. Volcano plot projection of DEGs in control myocyte vs myofiber populations – padj value of 0.05 used to establish the horizontal threshold (right). **C**. Volcano plot projection of Control vs Tet-On myocytes (left) and myofibers (right). P adjusted value cutoff is 0.05, and labeled genes are all significant DEGs. **D.** Heatmap projection of normalized gene expression values across myocyte and myofiber populations in Control and Tet-On samples (top). Population specific hits are labeled; Tet-On

804 regenerative hits, Control myocyte hits, and Control myofiber hits. Violin plot of normalized gene
805 expression for DEGs. P values included in this figure: $*p < 0.05$, $**p < 0.01$, $***p < 0.001$, $****p$
806 < 0.0001.

807 **Table S1: Spatial Transcriptomic Analysis Relevant to Figure 1**

808 9 tabs of data including (in order from left to right); SMPCs Day 1 vs Day 5, Day 5 vs Day 10,
809 Myocytes Day 1 vs Day 5, Day 5 vs Day 10, Day 10 vs Day 20, Human-only myofibers Day 10
810 vs Day 20, Chimeric myofibers Day 5 vs Day 10, Day 10 vs Day 20, and Human-only myofibers
811 vs Chimeric myofibers.

812 **Table S2: Spatial Transcriptomic Analysis Relevant to Figure 2 and 3**

813 8 tabs of data including (in order from left to right); Figure 2 PC1 top 200 genes both directions,
814 Figure 2 PC2 top 200 genes both directions, SMPCs WT vs MDX, Myofibers WT vs MDX, WT
815 SMPCs post vs pre, WT myofibers post vs pre, MDX SMPCs post vs pre, MDX myofibers post
816 vs pre-injury.

817 **Table S3: RNA-sequencing Analysis Relevant to Figure 5**

818 DESeq table of DEGs comparing Control to Tet-On MEGF10+ SMPCs.

819 **Table S4: Spatial Transcriptomic Analysis Relevant to Figure 7.**

820 4 tabs of data including (in order from left to right); SMPCs Tet-On vs Control, myocytes Tet-On
821 vs Control, myofibers Tet-On vs Control, Control myocyte vs myofibers.

822

823 **MATERIALS AND METHODS**

824 Cell Culture Techniques and CRISPR Homology Directed Repair

825 H1 hPSCs were used as the template cell line in this study to generate all CRISPR knock-
826 ins and control lines for engraftments. We harnessed sgRNA mediated CRISPR-HDR to generate
827 rtTA control insertion cell line and introduced EF1A-rtTA-mTagBFP2 transgene into the *AAVS1*

genomic safe harbor. We verified the insertion with flow cytometry, PCR, rtPCR validation techniques. Tet-On hPSCs had an additional insertion, the TET-MEGF10-TdTomato into the *ROSA26* locus, validated with flow cytometry and PCR. EMARDD Logan and Takayama disease modeling lines modeled patient variants described in literature, verified through PCR and sanger sequencing. hPSC lines were differentiated to skeletal muscle using our lab's publicly available protocol and enriching for SMPCs using ERBB3, HNK1, and NGFR. Fusion assays conducted using N2 differentiation media with TGFB inhibitor.

RNA Sequencing of SMPCs

We collected freshly enriched control and Tet-On SMPCs following directed differentiation. These samples were pelleted and RNA-extracted using the RNA-easy MicroPrep Kit (Qiagen). Following library preparation, we sequenced samples at ~60 million reads and fastq files were uploaded into Galaxy for fastQ grooming, HiSAT2 alignment, and generation of a counts matrix. We uploaded these matrices into R for differential gene expression analysis with DESeq2.

Skeletal Muscle Stem Cell Engraftments

Prior to engraftment, mice (MDXD2/WT) Pax7-Cre ROSA-DTA were treated with tamoxifen for a week to ablate endogenous Pax7 cells and treated with 50µL Barium Chloride into their tibialis anterior. Enriched SMPCs were passaged once to maximize the engraftments at 1.2million SMPCs per mouse. Tissues were harvested after engraftment by flash freezing in OCT and liquid nitrogen and stored at -80C. Tissues were then systematically sectioned in their entirety to determine the best region of engraftment. All engraftments consisted of an N=3.

GeoMX DSP Spatial Transcriptomic Analysis

Freshly sectioned engraftment samples were coated with Human Whole Transcriptome Probe Atlas (Bruker) and stained with antibodies of interest for ROI collection on the GeoMX DSP. Illumina sequencing at 2 million reads per micron yielded fastQ files, which were converted to DCC files, and uploaded into the GeoMX platform. We flagged and removed samples that failed

to meet standards for background noise (>90% genes below negative probe threshold) and proceeded with filtering the target datasets at 2% LOQ values. These raw counts files were uploaded into DESeq2 for downstream normalization and analysis.

DATA AVAILABILITY

RNA-sequencing data are available through NCBI GEO under accession GSE325461. Spatial transcriptomic data will be deposited in NCBI GEO, and spatial transcriptomic fluorescent and segmentation images will be deposited in the BioImage Archive.

REFERENCES

1. Sacco, A., F. Mourkioti, R. Tran, J. Choi, M. Llewellyn, P. Kraft, . . . H.M. Blau, *Short telomeres and stem cell exhaustion model Duchenne muscular dystrophy in mdx/mTR mice.* Cell, 2010. **143**(7): p. 1059-71.
2. Hwang, A.B. and A.S. Brack, *Muscle Stem Cells and Aging.* Curr Top Dev Biol, 2018. **126**: p. 299-322.
3. Mendell, J.R., J.T. Kissel, A.A. Amato, W. King, L. Signore, T.W. Prior, . . . et al., *Myoblast transfer in the treatment of Duchenne's muscular dystrophy.* N Engl J Med, 1995. **333**(13): p. 832-8.
4. Gussoni, E., G.K. Pavlath, A.M. Lanctot, K.R. Sharma, R.G. Miller, L. Steinman, and H.M. Blau, *Normal dystrophin transcripts detected in Duchenne muscular dystrophy patients after myoblast transplantation.* Nature, 1992. **356**(6368): p. 435-8.
5. Hicks, M., *Regenerating ACTC1 Human Myofibers Form an Emerging Niche to Support PAX7 Cells*. 2023: Nature Cell Biology.
6. Rayagiri, S.S., D. Ranaldi, A. Raven, N.I.F. Mohamad Azhar, O. Lefebvre, P.S. Zammit, and A.G. Borycki, *Basal lamina remodeling at the skeletal muscle stem cell niche mediates stem cell self-renewal.* Nat Commun, 2018. **9**(1): p. 1075.
7. Hicks, M.R. and A.D. Pyle, *The emergence of the stem cell niche.* Trends Cell Biol, 2022.
8. Brohl, D., E. Vasyutina, M.T. Czajkowski, J. Griger, C. Rassek, H.P. Rahn, . . . C. Birchmeier, *Colonization of the satellite cell niche by skeletal muscle progenitor cells depends on Notch signals.* Dev Cell, 2012. **23**(3): p. 469-81.
9. Young, C.S., M.R. Hicks, N.V. Ermolova, H. Nakano, M. Jan, S. Younesi, . . . A.D. Pyle, *A Single CRISPR-Cas9 Deletion Strategy that Targets the Majority of DMD Patients*

Restores Dystrophin Function in hiPSC-Derived Muscle Cells. Cell Stem Cell, 2016. **18**(4): p. 533-40.

10. Hicks, M.R., J. Hiserodt, K. Paras, W. Fujiwara, A. Eskin, M. Jan, . . . A.D. Pyle, *ERBB3 and NGFR mark a distinct skeletal muscle progenitor cell in human development and hPSCs.* Nat Cell Biol, 2018. **20**(1): p. 46-57.

11. Borchin, B., J. Chen, and T. Barberi, *Derivation and FACS-mediated purification of PAX3+/PAX7+ skeletal muscle precursors from human pluripotent stem cells.* Stem Cell Reports, 2013. **1**(6): p. 620-31.

12. Chal, J., M. Oginuma, Z. Al Tanoury, B. Gobert, O. Sumara, A. Hick, . . . O. Pourquie, *Differentiation of pluripotent stem cells to muscle fiber to model Duchenne muscular dystrophy.* Nat Biotechnol, 2015. **33**(9): p. 962-9.

13. Shelton, M., J. Metz, J. Liu, R.L. Carpenedo, S.P. Demers, W.L. Stanford, and I.S. Skerjanc, *Derivation and expansion of PAX7-positive muscle progenitors from human and mouse embryonic stem cells.* Stem Cell Reports, 2014. **3**(3): p. 516-29.

14. Xi, H., W. Fujiwara, K. Gonzalez, M. Jan, S. Liebscher, B. Van Handel, . . . A.D. Pyle, *In Vivo Human Somitogenesis Guides Somite Development from hPSCs.* Cell Rep, 2017. **18**(6): p. 1573-1585.

15. Jaime, O.G., J. Arias, S. Pavani, A.D. Pyle, and M.R. Hicks, *SIX1+PAX3+ identify a progenitor for myogenic lineage commitment from hPSCs.* Development, 2023. **150**(14).

16. Xi, H., J. Langerman, S. Sabri, P. Chien, C.S. Young, S. Younesi, . . . A.D. Pyle, *A Human Skeletal Muscle Atlas Identifies the Trajectories of Stem and Progenitor Cells across Development and from Human Pluripotent Stem Cells.* Cell Stem Cell, 2020. **27**(1): p. 158-176 e10.

17. Sun, C., S. Kannan, I.Y. Choi, H. Lim, H. Zhang, G.S. Chen, . . . G. Lee, *Human pluripotent stem cell-derived myogenic progenitors undergo maturation to quiescent satellite cells upon engraftment.* Cell Stem Cell, 2022. **29**(4): p. 610-619 e5.

18. Ganassi, M., F. Muntoni, and P.S. Zammit, *Defining and identifying satellite cell-opathies within muscular dystrophies and myopathies.* Exp Cell Res, 2022. **411**(1): p. 112906.

19. Kodippili, K. and M.A. Rudnicki, *Satellite cell contribution to disease pathology in Duchenne muscular dystrophy.* Front Physiol, 2023. **14**: p. 1180980.

20. Mazala, D.A.G., R. Hindupur, Y.J. Moon, F. Shaikh, I.H. Gamu, D. Alladi, . . . J.K. Jaiswal, *Altered muscle niche contributes to myogenic deficit in the D2-mdx model of severe DMD.* Cell Death Discov, 2023. **9**(1): p. 224.

21. Urciuolo, A., M. Quarta, V. Morbidoni, F. Gattazzo, S. Molon, P. Grumati, . . . P. Bonaldo, *Collagen VI regulates satellite cell self-renewal and muscle regeneration.* Nat Commun, 2013. **4**: p. 1964.

22. Logan, C.V., B. Lucke, C. Pottinger, Z.A. Abdelhamed, D.A. Parry, K. Szymanska, . . . C.A. Johnson, *Mutations in MEGF10, a regulator of satellite cell myogenesis, cause early onset myopathy, areflexia, respiratory distress and dysphagia (EMARDD).* Nat Genet, 2011. **43**(12): p. 1189-92.

23. Takayama, K., S. Mitsuhashi, J.Y. Shin, R. Tanaka, T. Fujii, R. Tsuburaya, . . . I. Nishino, *Japanese multiple epidermal growth factor 10 (MEGF10) myopathy with novel mutations: A phenotype-genotype correlation.* Neuromuscul Disord, 2016. **26**(9): p. 604-9.

24. Evano, B. and S. Tajbakhsh, *Skeletal muscle stem cells in comfort and stress.* NPJ Regen Med, 2018. **3**: p. 24.

25. Verma, M., Y. Asakura, X. Wang, K. Zhou, M. Unverdi, A.P. Kann, . . . A. Asakura, *Endothelial cell signature in muscle stem cells validated by VEGFA-FLT1-AKT1 axis promoting survival of muscle stem cell.* Elife, 2024. **13**.

26. Sampath, S.C., S.C. Sampath, A.T.V. Ho, S.Y. Corbel, J.D. Millstone, J. Lamb, . . . H.M. Blau, *Induction of muscle stem cell quiescence by the secreted niche factor Oncostatin M.* Nat Commun, 2018. **9**(1): p. 1531.

27. Cecchini, A., M. Loreti, C.D. Kaufman, C. Stamenkovic, G. Guarnaccia, A. Renero, . . . A. Sacco, *Tenascin-C from the tissue microenvironment promotes muscle stem cell maintenance and function through Annexin A2.* Commun Biol, 2025. **8**(1): p. 1709.

28. Hung, M., H.F. Lo, A.G. Beckmann, D. Demircioglu, G. Damle, D. Hasson, . . . R.S. Krauss, *Cadherin-dependent adhesion is required for muscle stem cell niche anchorage and maintenance.* Development, 2024. **151**(7).

29. Goel, A.J., M.K. Rieder, H.H. Arnold, G.L. Radice, and R.S. Krauss, *Niche Cadherins Control the Quiescence-to-Activation Transition in Muscle Stem Cells.* Cell Rep, 2017. **21**(8): p. 2236-2250.

30. Baghdadi, M.B., D. Castel, L. Machado, S.I. Fukada, D.E. Birk, F. Relaix, . . . P. Mourikis, *Reciprocal signalling by Notch-Collagen V-CALCR retains muscle stem cells in their niche.* Nature, 2018. **557**(7707): p. 714-718.

31. Yamaguchi, M., Y. Watanabe, T. Ohtani, A. Uezumi, N. Mikami, M. Nakamura, . . . S. Fukada, *Calcitonin Receptor Signaling Inhibits Muscle Stem Cells from Escaping the Quiescent State and the Niche.* Cell Rep, 2015. **13**(2): p. 302-14.

32. Clock, B. and M. Hicks, *Human Skeletal Muscle Niche Formation and Analysis with Spatial RNA Sequencing.* Methods Mol Biol, 2025.

33. Hernandez, S., R. Lazcano, A. Serrano, S. Powell, L. Kostousov, J. Mehta, . . . L.M. Solis, *Challenges and Opportunities for Immunoprofiling Using a Spatial High-Plex Technology: The NanoString GeoMx((R)) Digital Spatial Profiler.* Front Oncol, 2022. **12**: p. 890410.

34. Love, M.I., W. Huber, and S. Anders, *Moderated estimation of fold change and dispersion for RNA-seq data with DESeq2.* Genome Biol, 2014. **15**(12): p. 550.

35. Low, S., J.L. Barnes, P.S. Zammit, and J.R. Beauchamp, *Delta-Like 4 Activates Notch 3 to Regulate Self-Renewal in Skeletal Muscle Stem Cells.* Stem Cells, 2018. **36**(3): p. 458-466.

36. Barruet, E., S.M. Garcia, J. Wu, B.M. Morales, S. Tamaki, T. Moody, . . . E.C. Hsiao, *Modeling the ACVR1(R206H) mutation in human skeletal muscle stem cells.* Elife, 2021. **10**.

37. Zhang, Y., I. Lahmann, K. Baum, H. Shimojo, P. Mourikis, J. Wolf, . . . C. Birchmeier, *Oscillations of Delta-like1 regulate the balance between differentiation and maintenance of muscle stem cells.* Nat Commun, 2021. **12**(1): p. 1318.

38. Lapan, A.D., A. Rozkalne, and E. Gussoni, *Human fetal skeletal muscle contains a myogenic side population that expresses the melanoma cell-adhesion molecule.* Hum Mol Genet, 2012. **21**(16): p. 3668-80.

39. Petrany, M.J., T. Song, S. Sadayappan, and D.P. Millay, *Myocyte-derived Myomaker expression is required for regenerative fusion but exacerbates membrane instability in dystrophic myofibers.* JCI Insight, 2020. **5**(9).

40. Schiaffino, S., A.C. Rossi, V. Smerdu, L.A. Leinwand, and C. Reggiani, *Developmental myosins: expression patterns and functional significance.* Skelet Muscle, 2015. **5**: p. 22.

41. Shiura, H., M. Kitazawa, F. Ishino, and T. Kaneko-Ishino, *Roles of retrovirus-derived PEG10 and PEG11/RTL1 in mammalian development and evolution and their involvement in human disease.* Front Cell Dev Biol, 2023. **11**: p. 1273638.

42. Andersen, D.C., J. Laborda, V. Baladron, M. Kassem, S.P. Sheikh, and C.H. Jensen, *Dual role of delta-like 1 homolog (DLK1) in skeletal muscle development and adult muscle regeneration.* Development, 2013. **140**(18): p. 3743-53.

43. Xu, X., Z. Yu, N. Ai, S. Liufu, X. Liu, B. Chen, . . . Y. Yin, *Molecular Mechanism of MYL4 Regulation of Skeletal Muscle Development in Pigs.* Genes (Basel), 2023. **14**(6).

44. Walter, L.D., J.L. Orton, I. Ntekas, E.H.H. Fong, V.I. Maymi, B.D. Rudd, . . . B.D. Cosgrove, *Transcriptomic analysis of skeletal muscle regeneration across mouse lifespan identifies altered stem cell states.* Nat Aging, 2024. **4**(12): p. 1862-1881.

45. Endo, Y., C.D. Hwang, Y. Zhang, S. Olumi, D.J. Koh, C. Zhu, . . . I. Sinha, *VEGFA Promotes Skeletal Muscle Regeneration in Aging.* Adv Biol (Weinh), 2023. **7**(10): p. e2200320.

46. Hitachi, K., Y. Kiyofuji, H. Yamaguchi, M. Nakatani, M. Inui, and K. Tsuchida, *Simultaneous loss of skeletal muscle myosin heavy chain IIx and IIb causes severe skeletal muscle hypoplasia in postnatal mice.* FASEB J, 2023. **37**(1): p. e22692.

47. Coley, W.D., L. Bogdanik, M.C. Vila, Q. Yu, J.H. Van Der Meulen, S. Rayavarapu, . . . K. Nagaraju, *Effect of genetic background on the dystrophic phenotype in mdx mice.* Hum Mol Genet, 2016. **25**(1): p. 130-45.

48. Waingankar, T.P. and P. D'Silva, *Multiple variants of the human presequence translocase motor subunit Magmas govern the mitochondrial import.* J Biol Chem, 2021. **297**(6): p. 101349.

49. Chen, W.J., I.H. Lin, C.W. Lee, and Y.F. Chen, *Aged Skeletal Muscle Retains the Ability to Remodel Extracellular Matrix for Degradation of Collagen Deposition after Muscle Injury.* Int J Mol Sci, 2021. **22**(4).

50. Wu, L., L. Wang, Y. Zhuang, Y. Luo, Q. Zhu, M. Maimaitizunong, . . . W. Ren, *Integrative analysis reveals synergistic regulation of Sp7 by BRD9 and Wnt/beta-catenin signaling during osteogenic differentiation.* Commun Biol, 2025. **9**(1): p. 23.

51. Merrick, M.A., *Secondary injury after musculoskeletal trauma: a review and update.* J Athl Train, 2002. **37**(2): p. 209-17.

52. Perez-Diaz, S., Z. Koumaiha, M.J. Borok, F. Aurade, M. Pini, B. Periou, . . . F. Relaix, *Obesity impairs skeletal muscle repair through NID-1 mediated extracellular matrix remodeling by mesenchymal progenitors.* Matrix Biol, 2022. **112**: p. 90-115.

53. Guo, J., D. Ma, R. Huang, J. Ming, M. Ye, K. Kee, . . . J. Na, *An inducible CRISPR-ON system for controllable gene activation in human pluripotent stem cells.* Protein Cell, 2017. **8**(5): p. 379-393.

54. Papapetrou, E.P. and A. Schambach, *Gene Insertion Into Genomic Safe Harbors for Human Gene Therapy.* Mol Ther, 2016. **24**(4): p. 678-84.

55. Relaix, F., D. Rocancourt, A. Mansouri, and M. Buckingham, *A Pax3/Pax7-dependent population of skeletal muscle progenitor cells.* Nature, 2005. **435**(7044): p. 948-53.

56. Hu, Y., Y. Zhang, J. He, H. Rao, Z. Wei, Z. Shen, and C. Zhou, *HMMR in human cancers: regulatory mechanism and biological function.* J Transl Med, 2025. **23**(1): p. 1302.

57. Chung, S., E. Sperier, K. Graciano, X. Hu, H. Guo, and J. Xu, *Aurora kinases, emerging critical targets for cancer treatment and related new therapeutic strategies.* Bioorg Chem, 2025. **163**: p. 108633.

58. Barad, M., F. Csukasi, M. Bosakova, J.H. Martin, W. Zhang, S. Paige Taylor, . . . I. Duran, *Biallelic mutations in LAMA5 disrupts a skeletal noncanonical focal adhesion pathway and produces a distinct bent bone dysplasia.* EBioMedicine, 2020. **62**: p. 103075.

59. Biressi, S., A. Filareto, and T.A. Rando, *Stem cell therapy for muscular dystrophies.* J Clin Invest, 2020. **130**(11): p. 5652-5664.

60. Tabebordbar, M., K. Zhu, J.K.W. Cheng, W.L. Chew, J.J. Widrick, W.X. Yan, . . . A.J. Wagers, *In vivo gene editing in dystrophic mouse muscle and muscle stem cells.* Science, 2016. **351**(6271): p. 407-411.

61. Meng, J., M. Bencze, R. Asfahani, F. Muntoni, and J.E. Morgan, *The effect of the muscle environment on the regenerative capacity of human skeletal muscle stem cells.* Skelet Muscle, 2015. **5**: p. 11.

62. Stearns-Reider, K.M., M.R. Hicks, K.G. Hammond, J.C. Reynolds, A. Maity, Y.Z. Kurmangaliyev, . . . R.H. Crosbie, *Myoscaffolds reveal laminin scarring is detrimental for stem cell function while sarcospan induces compensatory fibrosis.* NPJ Regen Med, 2023. **8**(1): p. 16.

63. Crist, S.B., K. Azzag, J. Kiley, I. Coleman, A. Magli, and R.C.R. Perlingeiro, *The adult environment promotes the transcriptional maturation of human iPSC-derived muscle grafts.* NPJ Regen Med, 2024. **9**(1): p. 16.

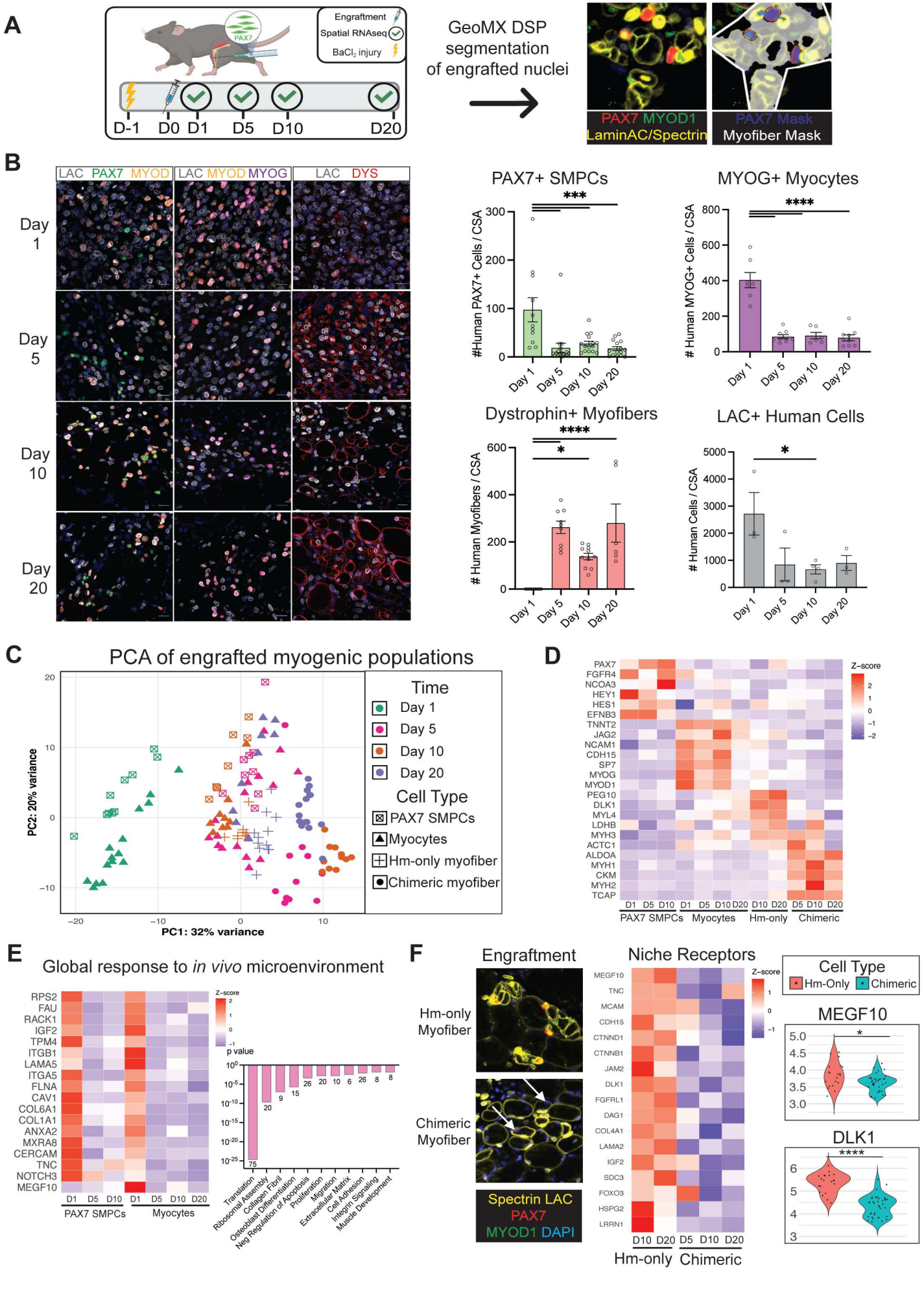
64. Muir, L.A., C.E. Murry, and J.S. Chamberlain, *Prosurvival Factors Improve Functional Engraftment of Myogenically Converted Dermal Cells into Dystrophic Skeletal Muscle.* Stem Cells Dev, 2016. **25**(20): p. 1559-1569.

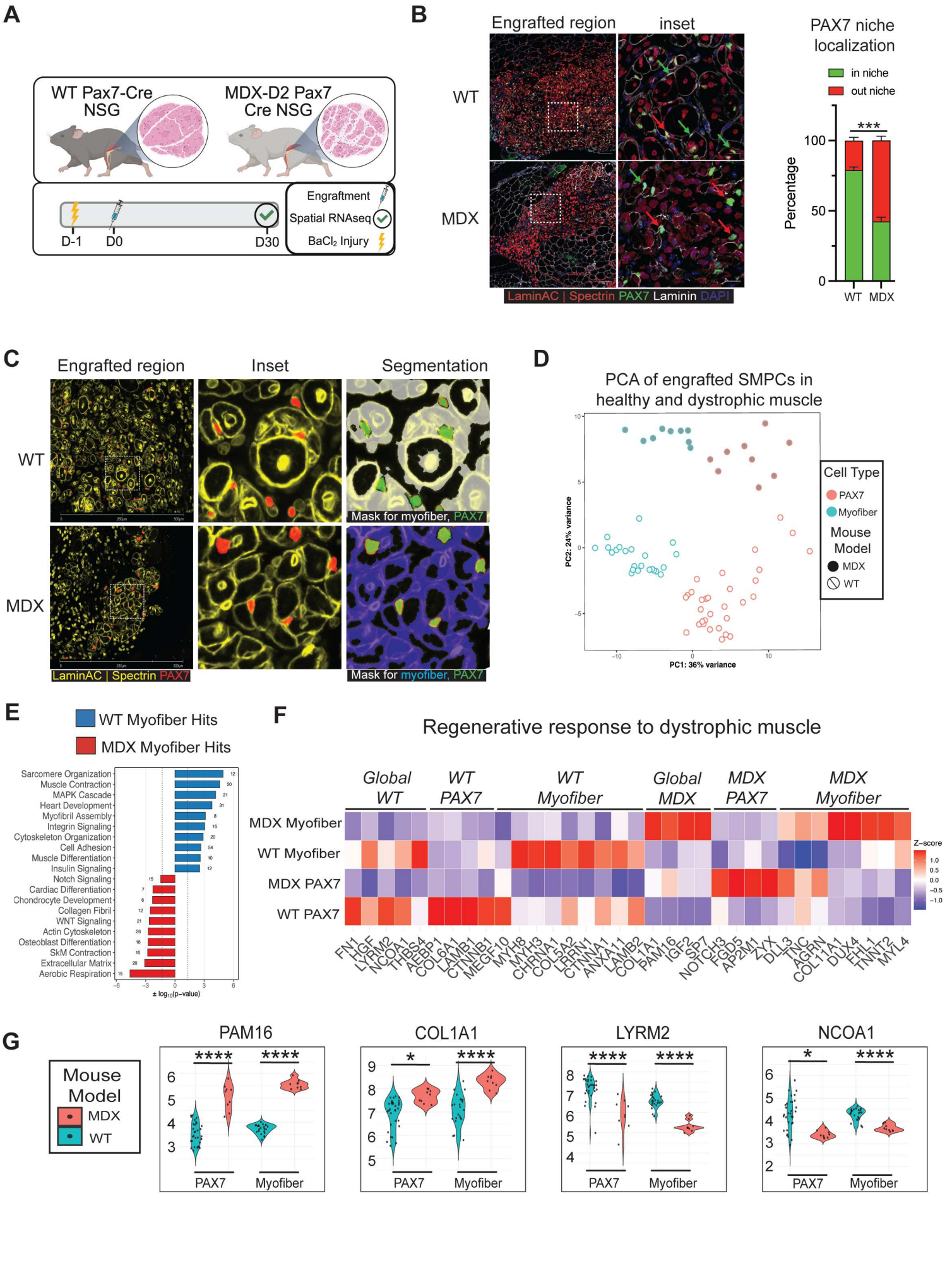
65. Cutler, A.A., B. Pawlikowski, J.R. Wheeler, N. Dalla Betta, T. Elston, R. O'Rourke, . . . B.B. Olwin, *The regenerating skeletal muscle niche drives satellite cell return to quiescence.* iScience, 2022. **25**(6): p. 104444.

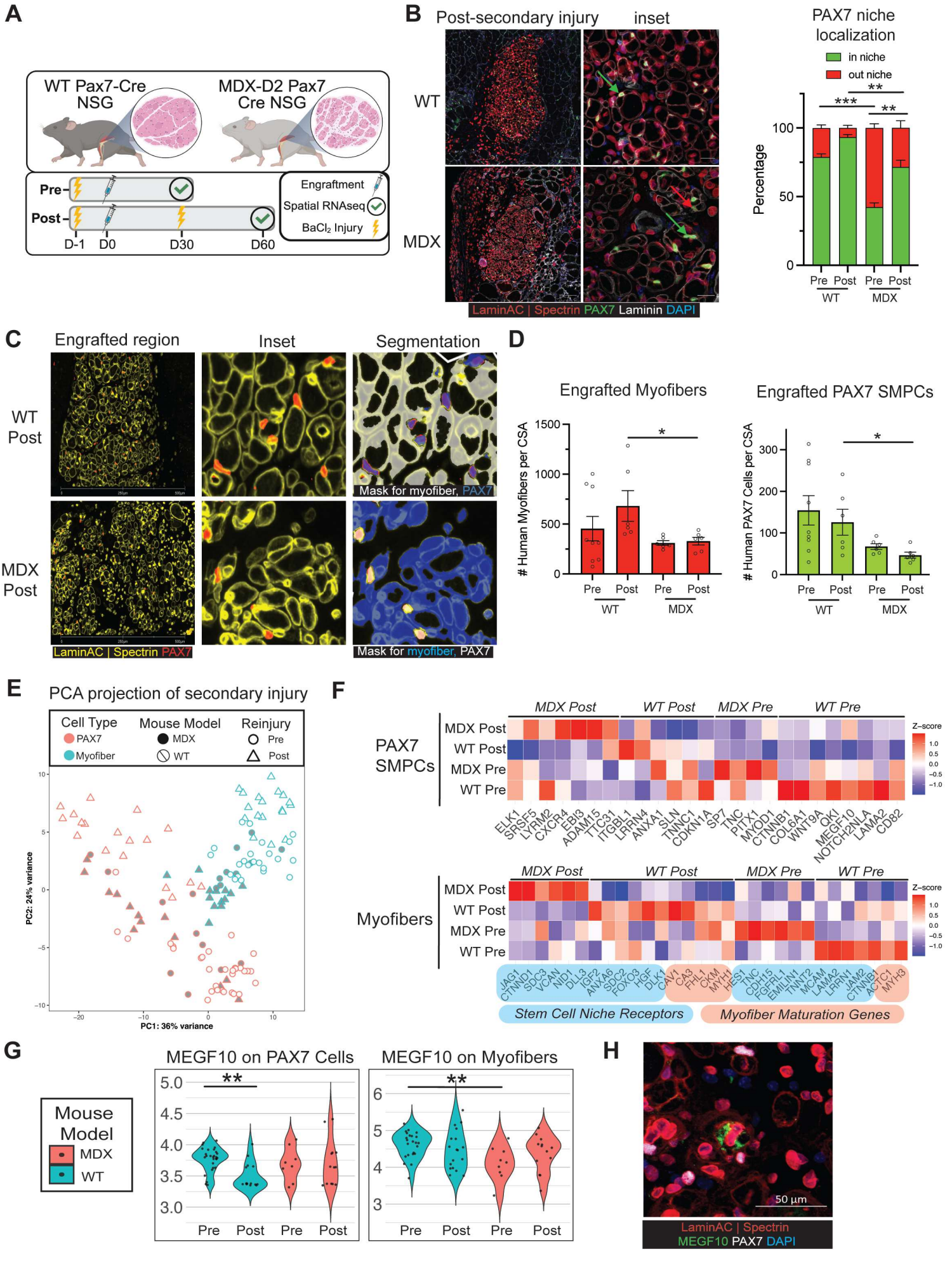
66. Iram, T., Z. Ramirez-Ortiz, M.H. Byrne, U.A. Coleman, N.D. Kingery, T.K. Means, . . . J. El Khoury, *Megf10 Is a Receptor for C1Q That Mediates Clearance of Apoptotic Cells by Astrocytes.* J Neurosci, 2016. **36**(19): p. 5185-92.

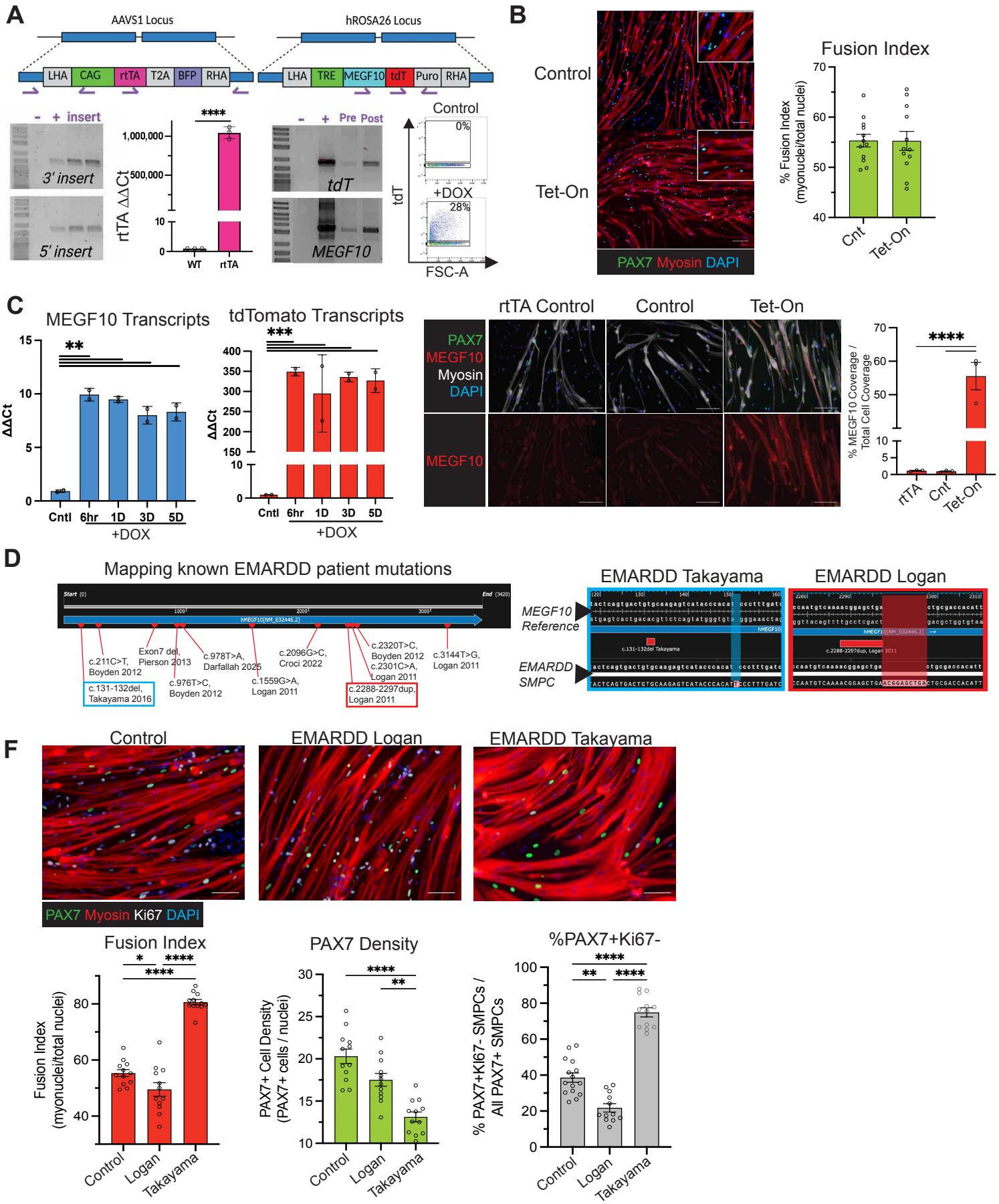
67. Ma, Q., X. Zhang, and J. Pan, *A cell atlas of multiple liver organoids and the fetal liver based on scRNA-seq.* iScience, 2026. **29**(3): p. 114955.

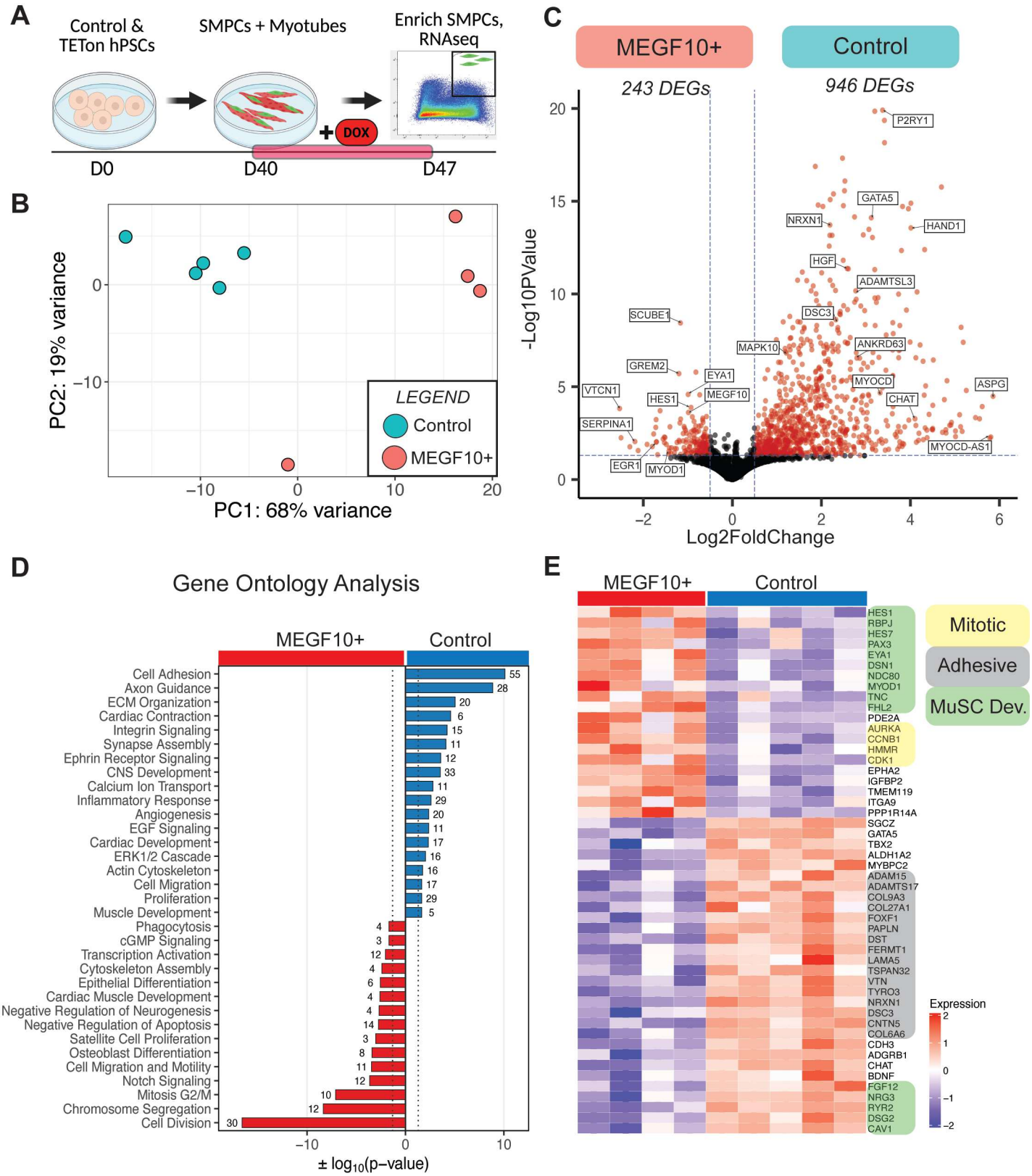
68. Haines, B.P., R. Gupta, C.M. Jones, D. Summerbell, and P.W. Rigby, *The NLRR gene family and mouse development: Modified differential display PCR identifies NLRR-1 as a gene expressed in early somitic myoblasts.* Dev Biol, 2005. **281**(2): p. 145-59.

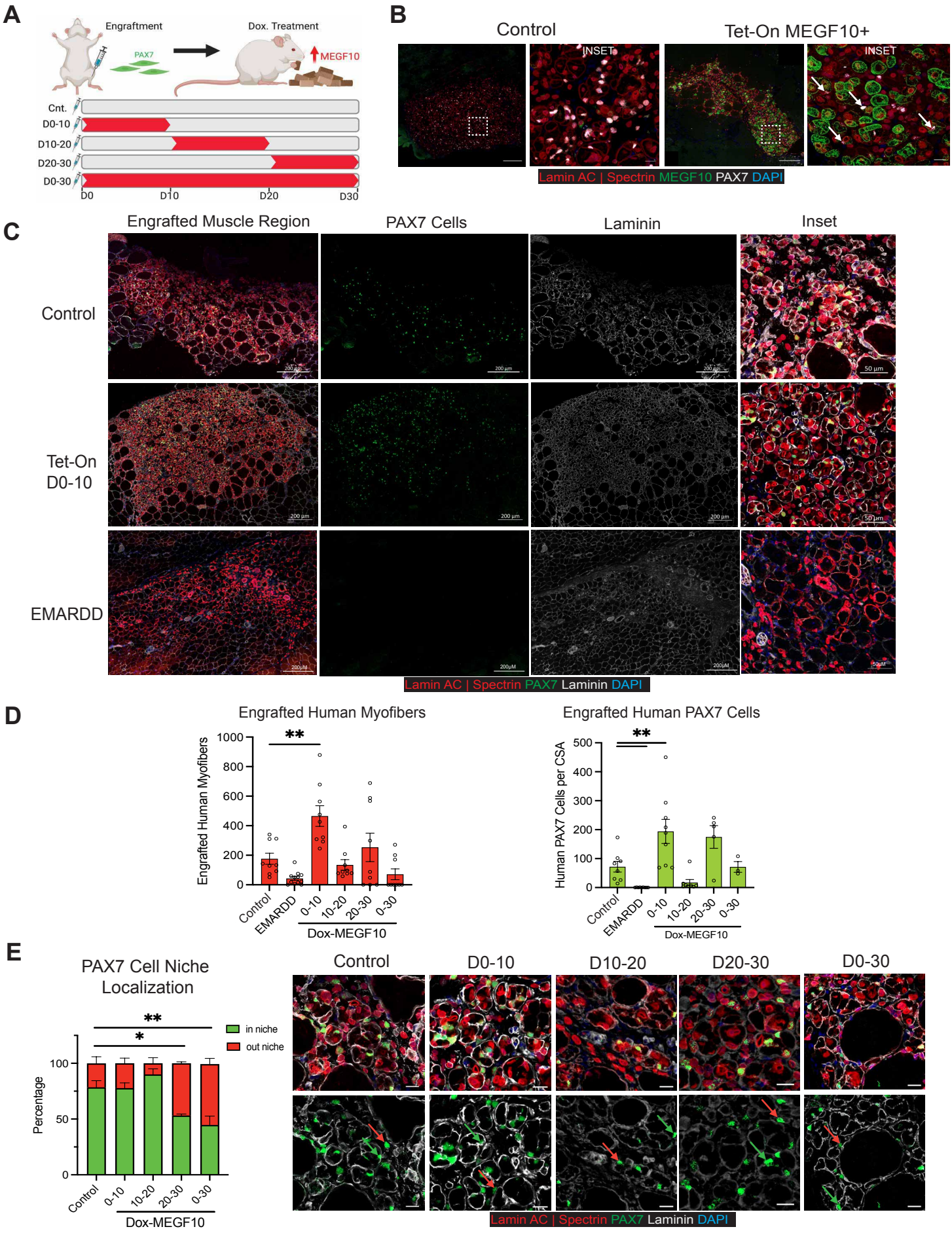

A
Engraftment
Spatial RNAseq
BaCl2 injury
PAX7
D-1
D0
D1
D5
D10
D20
GeoMX DSP
segmentation
of engrafted nuclei
PAX7 MYOD1
LaminAC/Spectrin
PAX7 Mask
Myofiber Mask
B
LAC PAX7 MYOD
LAC MYOD MYOG
LAC DYS
Day 1
Day 5
Day 10
Day 20
PAX7+ SMPCs
#Human PAX7+ Cells / CSA
MYOG+ Myocytes
Human MYOG+ Cells / CSA
Dystrophin+ Myofibers
Human Myofibers / CSA
LAC+ Human Cells
Human Cells / CSA
C
PCA of engrafted myogenic populations
PC2: 20% variance
PC1: 32% variance
Time
Day 1
Day 5
Day 10
Day 20
Cell Type
PAX7 SMPCs
Myocytes
Hm-only myofiber
Chimeric myofiber
D
Z-score
PAX7
FGFR4
NCOA3
HEY1
HES1
EFNB3
TNNT2
JAG2
NCAM1
CDH15
SP7
MYOG
MYOD1
PEG10
DLK1
MYL4
LDHB
MYH3
ACTC1
ALDOA
MYH1
CKM
MYH2
TCAP
PAX7 SMPCs
Myocytes
Hm-only
Chimeric
E
Global response to in vivo microenvironment
RPS2
FAU
RACK1
IGF2
TPM4
ITGB1
LAMA5
ITGA5
FLNA
CAV1
COL6A1
COL1A1
ANXA2
MXRA8
CERCAM
TNC
NOTCH3
MEGF10
PAX7 SMPCs
Myocytes
p value
Translation
Ribosomal Assembly
Collagen Fibril
Osteoblast Differentiation
Neg Regulation of Apoptosis
Proliferation
Migration
Extracellular Matrix
Cell Adhesion
Integrin Signaling
Muscle Development
F
Engraftment
Hm-only
Myofiber
Chimeric
Myofiber
Spectrin LAC
PAX7
MYOD1 DAPI
Niche Receptors
MEGF10
TNC
MCAM
CDH15
CTNND1
CTNNB1
JAM2
DLK1
FGFRL1
DAG1
COL4A1
LAMA2
IGF2
SDC3
FOXO3
HSPG2
LRRN1
Hm-only
Chimeric
Cell Type
Hm-Only
Chimeric
MEGF10
DLK1

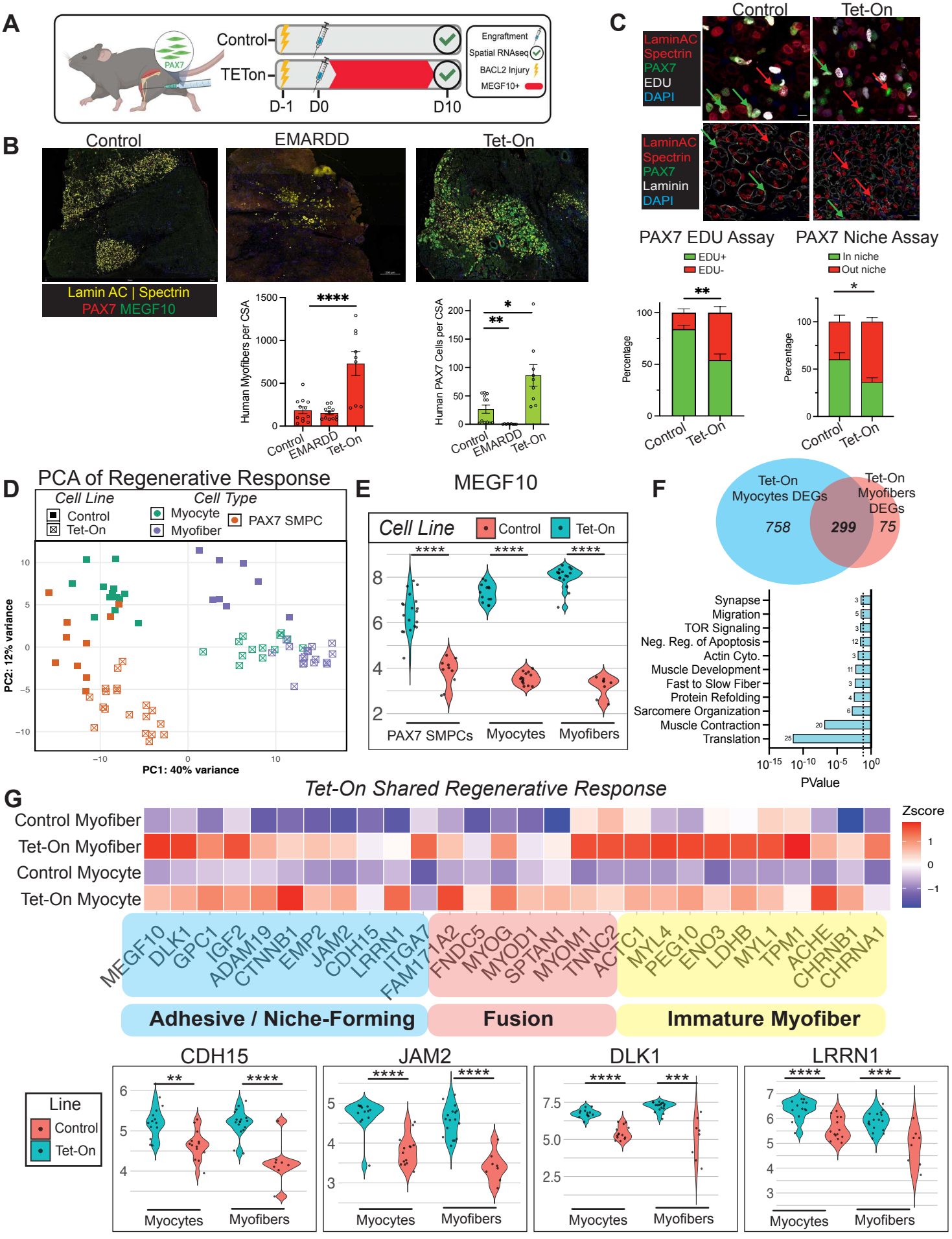

A
WT Pax7-Cre NSG
MDX-D2 Pax7 Cre NSG
Engraftment
Spatial RNAseq
BaCl2 Injury
D-1
D0
D30
B
Engrafted region
inset
WT
MDX
LaminAC | Spectrin PAX7 Laminin DAPI
PAX7 niche localization
in niche
out niche
***
Percentage
100
50
0
WT MDX
C
Engrafted region
Inset
Segmentation
WT
MDX
LaminAC | Spectrin PAX7
Mask for myofiber, PAX7
Mask for myofiber, PAX7
D
PCA of engrafted SMPCs in healthy and dystrophic muscle
PC2: 24% variance
PC1: 36% variance
Cell Type
PAX7
Myofiber
Mouse Model
MDX
WT
E
WT Myofiber Hits
MDX Myofiber Hits
Sarcomere Organization
Muscle Contraction
MAPK Cascade
Heart Development
Myofibril Assembly
Integrin Signaling
Cytoskeleton Organization
Cell Adhesion
Muscle Differentiation
Insulin Signaling
Notch Signaling
Cardiac Differentiation
Chondrocyte Development
Collagen Fibril
WNT Signaling
Actin Cytoskeleton
Osteoblast Differentiation
SkM Contraction
Extracellular Matrix
Aerobic Respiration
± log10(p-value)
F
Regenerative response to dystrophic muscle
Global WT
WT PAX7
WT Myofiber
Global MDX
MDX PAX7
MDX Myofiber
MDX Myofiber
WT Myofiber
MDX PAX7
WT PAX7
Z-score
FN1 HGF LYRM2 NCOA1 THBS4 AEBP1 COL6A1 LAMB1 CTNNB1 MEGF10 MYH8 MYH3 CHRNA1 COL5A2 LRRN1 CTNNA1 ANXA11 LAMB2 COL1A1 PAM16 IGF2 SP7 NOTCH3 FGD5 AP2M1 ZYX DLL3 TNC AGRN COL11A1 DUX4 EHL1 TNNT2 MYL4
G
Mouse Model
MDX
WT
PAM16
COL1A1
LYRM2
NCOA1
****
*
PAX7
Myofiber


A
WT Pax7-Cre NSG
MDX-D2 Pax7 Cre NSG
Pre
Post
D-1
D0
D30
D60
Engraftment
Spatial RNAseq
BaCl2 Injury
B
Post-secondary injury
inset
WT
MDX
LaminAC | Spectrin PAX7 Laminin DAPI
PAX7 niche localization
in niche
out niche
Percentage
Pre Post Pre Post
WT
MDX
C
Engrafted region
Inset
Segmentation
WT Post
MDX Post
Mask for myofiber, PAX7
LaminAC | Spectrin PAX7
D
Engrafted Myofibers
Human Myofibers per CSA
Engrafted PAX7 SMPCs
Human PAX7 Cells per CSA
E
PCA projection of secondary injury
Cell Type
PAX7
Myofiber
Mouse Model
MDX
WT
Reinjury
Pre
Post
PC2: 24% variance
PC1: 36% variance
F
PAX7 SMPCs
Myofibers
MDX Post
WT Post
MDX Pre
WT Pre
Z-score
ELK1 SRSF5 LYRM2 CXCR4 EBI3 ADAM15 TTC31 ITGBL1 LRRN4 ANXA1 SLN TNNC1 CDKN1A SP7 TNC PITX1 MYOD1 CTNNB1 COL6A1 WNT9A QKI MEGF10 NOTCH2NLA LAMA2 CD82
JAG1 CTNND1 SDC3 VCAN NID1 DLL3 IGF2 ANXA6 SDC2 FOXO3 HGF DLK1 CAV1 CA3 FHL1 CKM MYH1 HES1 TNC CDH15 FGFRL1 EMILIN1 TNNT2 MCAM LAMA2 LRRN1 JAM2 CTNNB1 ACTC1 MYH3
Stem Cell Niche Receptors
Myofiber Maturation Genes
G
Mouse Model
MDX
WT
MEGF10 on PAX7 Cells
MEGF10 on Myofibers
Pre Post Pre Post
H
50 µm
LaminAC | Spectrin
MEGF10 PAX7 DAPI

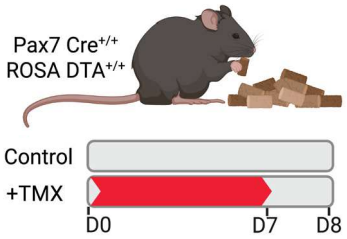

A
AAVS1 Locus
hROSA26 Locus
LHA
CAG
rtTA
T2A
BFP
RHA
LHA
TRE
MEGF10
tdT
Puro
RHA
- + insert
3' insert
5' insert
****
rtTA ΔΔCt
1,000,000
500,000
10
0
WT
rtTA
- + Pre Post
tdT
MEGF10
Control
0%
+DOX
28%
tdT
FSC-A
B
Control
Tet-On
PAX7 Myosin DAPI
Fusion Index
% Fusion Index (myonuclei/total nuclei)
70
60
50
40
Cnt
Tet-On
C
MEGF10 Transcripts
**
ΔΔCt
15
10
5
0
Cntl
6hr
1D
3D
5D
+DOX
tdTomato Transcripts
***
ΔΔCt
400
350
300
250
200
150
10
0
Cntl
6hr
1D
3D
5D
+DOX
rtTA Control
Control
Tet-On
PAX7
MEGF10
Myosin
DAPI
MEGF10
****
% MEGF10 Coverage / Total Cell Coverage
70
60
50
10
5
0
rtTA
Cnt
Tet-On
D
Mapping known EMARDD patient mutations
Start (0)
End (3420)
1000
2000
3000
hMEGF10(NM_032446.2)
c.211C>T, Boyden 2012
Exon7 del, Pierson 2013
c.978T>A, Darfallah 2025
c.2096G>C, Croci 2022
c.2320T>C, Boyden 2012
c.2301C>A, Logan 2011
c.3144T>G, Logan 2011
c.131-132del, Takayama 2016
c.976T>C, Boyden 2012
c.1559G>A, Logan 2011
c.2288-2297dup, Logan 2011
EMARDD Takayama
EMARDD Logan
MEGF10 Reference
EMARDD SMPC
c.131-132del Takayama
c.2288-2297dup, Logan 2011
F
Control
EMARDD Logan
EMARDD Takayama
PAX7 Myosin Ki67 DAPI
Fusion Index
*
****
****
Fusion Index (myonuclei/total nuclei)
80
60
40
Control
Logan
Takayama
PAX7 Density
****
**
PAX7+ Cell Density (PAX7+ cells / nuclei)
30
25
20
15
10
Control
Logan
Takayama
%PAX7+Ki67-
****
**
****
% PAX7+Ki67- SMPCs / All PAX7+ SMPCs
100
80
60
40
20
0
Control
Logan
Takayama

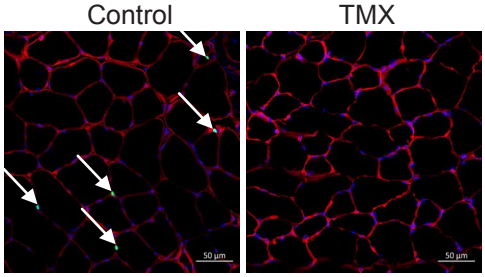

A
Control & TETon hPSCs
SMPCs + Myotubes
Enrich SMPCs, RNAseq
DOX
D0
D40
D47
B
PC2: 19% variance
PC1: 68% variance
LEGEND
Control
MEGF10+
C
MEGF10+
Control
243 DEGs
946 DEGs
-Log10PValue
Log2FoldChange
P2RY1
GATA5
NRXN1
HAND1
HGF
ADAMTSL3
DSC3
SCUBE1
MAPK10
ANKRD63
GREM2
EYA1
MYOCD
VTCN1
HES1
MEGF10
CHAT
ASPG
SERPINA1
MYOCD-AS1
EGR1
MYOD1
D
Gene Ontology Analysis
MEGF10+
Control
Cell Adhesion 55
Axon Guidance 28
ECM Organization 20
Cardiac Contraction 6
Integrin Signaling 15
Synapse Assembly 11
Ephrin Receptor Signaling 12
CNS Development 33
Calcium Ion Transport 11
Inflammatory Response 29
Angiogenesis 20
EGF Signaling 11
Cardiac Development 17
ERK1/2 Cascade 16
Actin Cytoskeleton 16
Cell Migration 17
Proliferation 29
Muscle Development 5
Phagocytosis 4
cGMP Signaling 3
Transcription Activation 12
Cytoskeleton Assembly 4
Epithelial Differentiation 6
Cardiac Muscle Development 4
Negative Regulation of Neurogenesis 4
Negative Regulation of Apoptosis 14
Satellite Cell Proliferation 3
Osteoblast Differentiation 8
Cell Migration and Motility 11
Notch Signaling 12
Mitosis G2/M 10
Chromosome Segregation 12
Cell Division 30
± log10(p–value)
E
MEGF10+
Control
HES1
RBPJ
HES7
PAX3
EYA1
DSN1
NDC80
MYOD1
TNC
FHL2
PDE2A
AURKA
CCNB1
HMMR
CDK1
EPHA2
IGFBP2
TMEM119
ITGA9
PPP1R14A
SGCZ
GATA5
TBX2
ALDH1A2
MYBPC2
ADAM15
ADAMTS17
COL9A3
COL27A1
FOXF1
PAPLN
DST
FERMT1
LAMA5
TSPAN32
VTN
TYRO3
NRXN1
DSC3
CNTN5
COL6A6
CDH3
ADGRB1
CHAT
BDNF
FGF12
NRG3
RYR2
DSG2
CAV1
Mitotic
Adhesive
MuSC Dev.
Expression

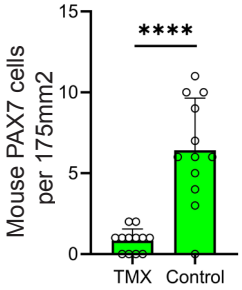

A
Engraftment
Dox. Treatment
PAX7
MEGF10
Cnt.
D0-10
D10-20
D20-30
D0-30
D0
D10
D20
D30
B
Control
Tet-On MEGF10+
INSET
INSET
Lamin AC | Spectrin MEGF10 PAX7 DAPI
C
Engrafted Muscle Region
PAX7 Cells
Laminin
Inset
Control
Tet-On D0-10
EMARDD
Lamin AC | Spectrin PAX7 Laminin DAPI
D
Engrafted Human Myofibers
Engrafted Human Myofibers
Control
EMARDD
0-10
10-20
20-30
0-30
Dox-MEGF10
Engrafted Human PAX7 Cells
Human PAX7 Cells per CSA
E
PAX7 Cell Niche Localization
in niche
out niche
Percentage
Control
D0-10
D10-20
D20-30
D0-30
Lamin AC | Spectrin PAX7 Laminin DAPI


A
Control
TETon
D-1
D0
D10
Engraftment
Spatial RNAseq
BACL2 Injury
MEGF10+
B
Control
EMARDD
Tet-On
Lamin AC | Spectrin
PAX7 MEGF10
Human Myofibers per CSA
Human PAX7 Cells per CSA
C
Control
Tet-On
LaminAC
Spectrin
PAX7
EDU
DAPI
Laminin
PAX7 EDU Assay
PAX7 Niche Assay
EDU+
EDU-
In niche
Out niche
Percentage
D
PCA of Regenerative Response
Cell Line
Control
Tet-On
Cell Type
Myocyte
Myofiber
PAX7 SMPC
PC1: 40% variance
PC2: 12% variance
E
MEGF10
PAX7 SMPCs
Myocytes
Myofibers
F
Tet-On Myocytes DEGs
Tet-On Myofibers DEGs
758
299
75
Synapse
Migration
TOR Signaling
Neg. Reg. of Apoptosis
Actin Cyto.
Muscle Development
Fast to Slow Fiber
Protein Refolding
Sarcomere Organization
Muscle Contraction
Translation
PValue
G
Tet-On Shared Regenerative Response
Control Myofiber
Tet-On Myofiber
Control Myocyte
Tet-On Myocyte
Zscore
MEGF10 DLK1 GPC1 IGF2 ADAM19 CTNNB1 EMP2 JAM2 CDH15 LRRN1 ITGA7 FAM171A2
FNDC5 MYOG MYOD1 SPTAN1 MYOM1 TNNC2 ACTC1
MYL4 PEG10 ENO3 LDHB MYL1 TPM1 ACHE CHRNB1 CHRNA1
Adhesive / Niche-Forming
Fusion
Immature Myofiber
CDH15
JAM2
DLK1
LRRN1
Line
Control
Tet-On
Myocytes
Myofibers

A



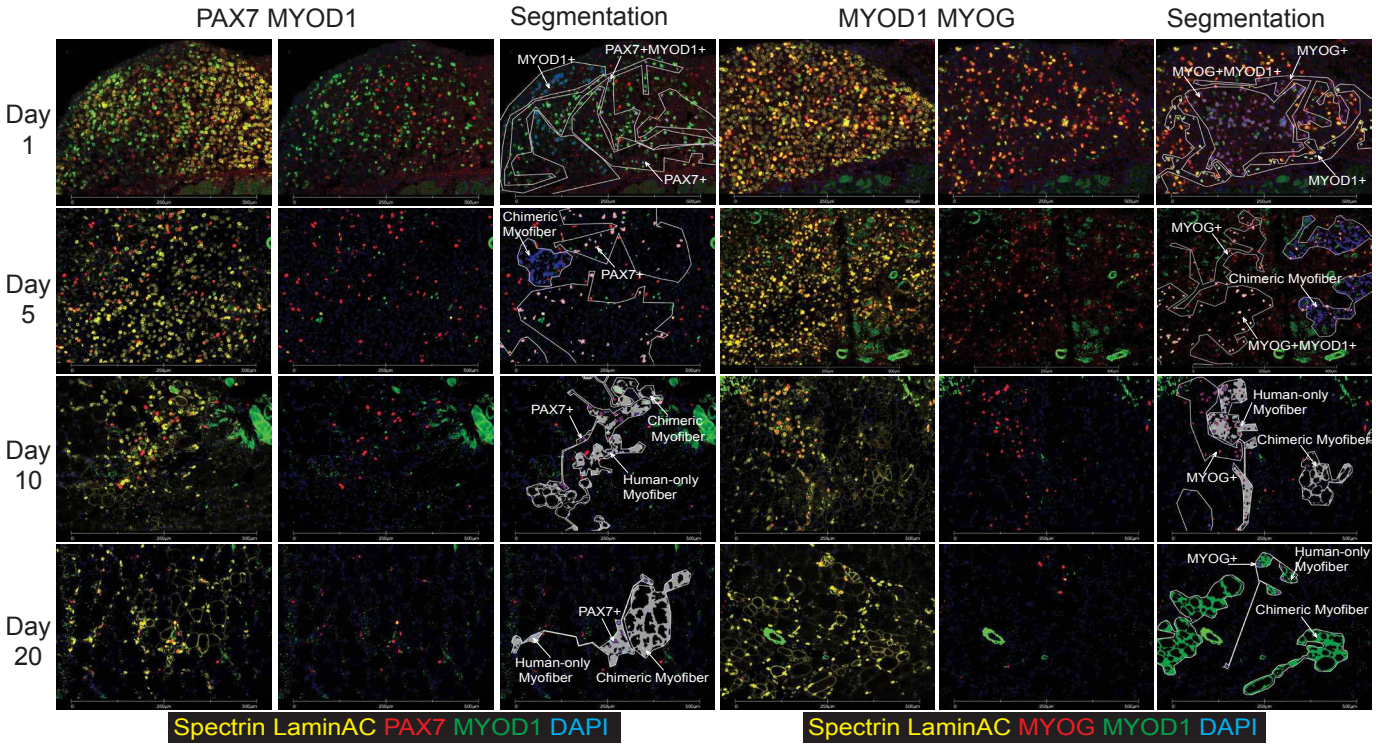




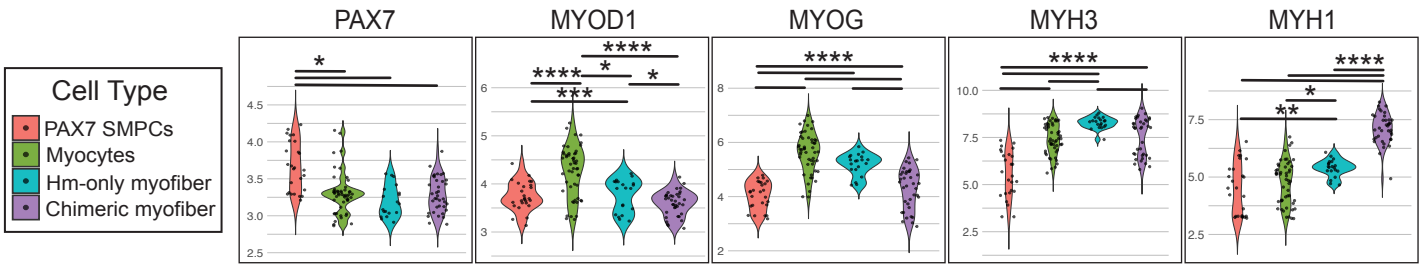
B

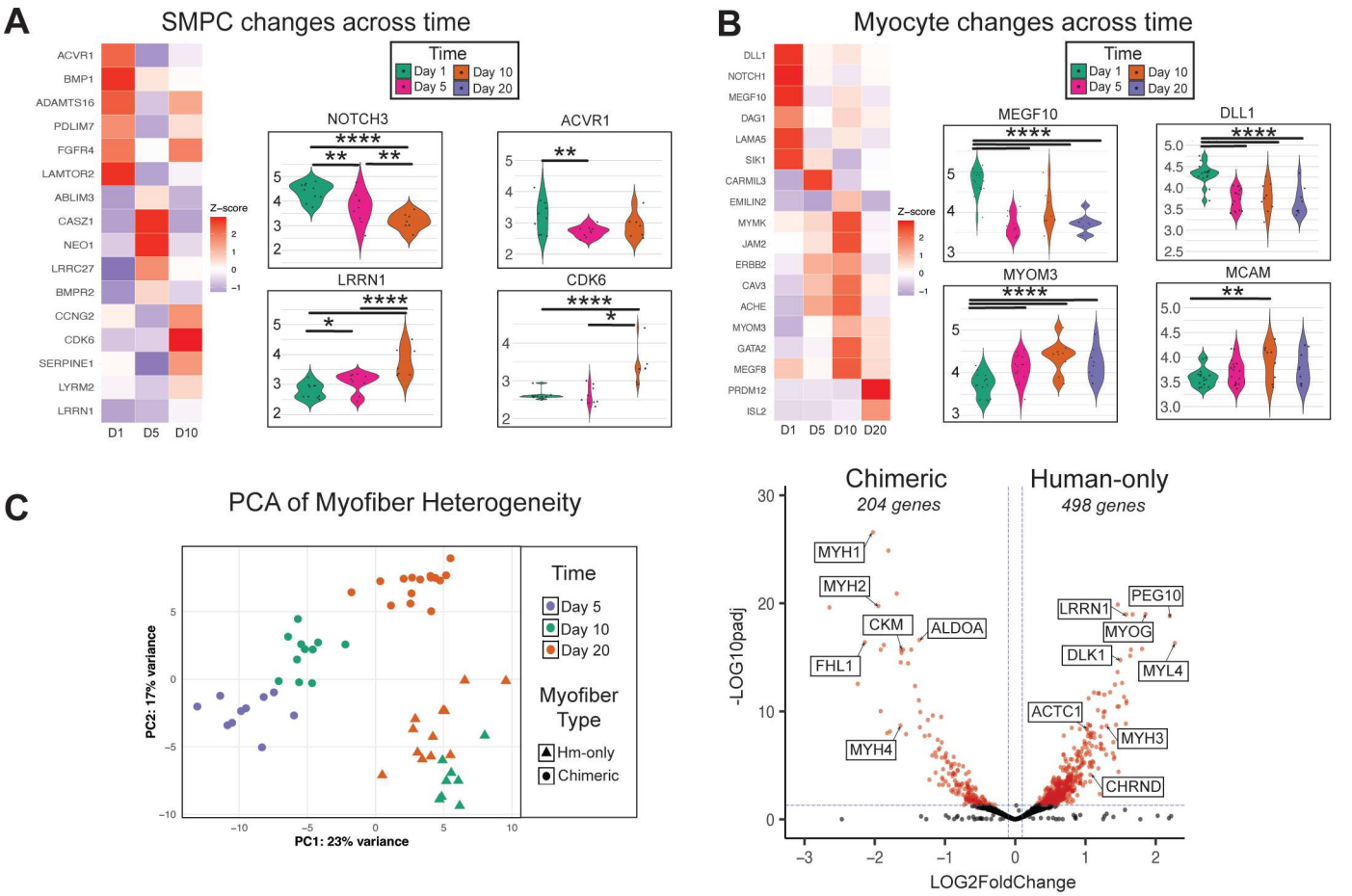
Time point	ROIs Collected				Total
	PAX7, PAX7/MYOD	MYOD/MYOG, MYOG	Human-Only	Chimeric	
Day 1	13	15	0	0	40
Day 5	13	18	6	5	42
Day 10	6	9	8	11	38
Day 20	8	12	12	15	47

C



D

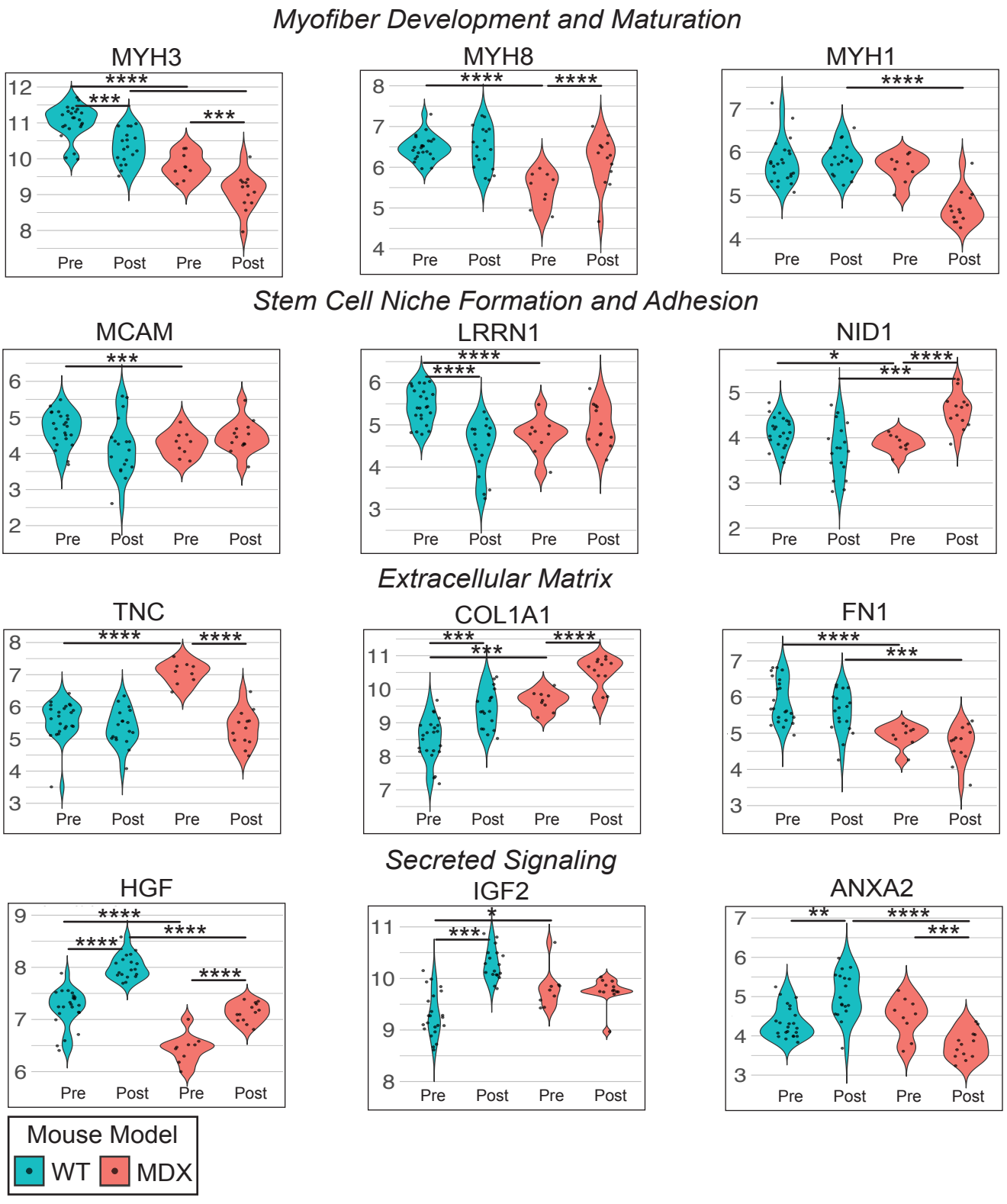


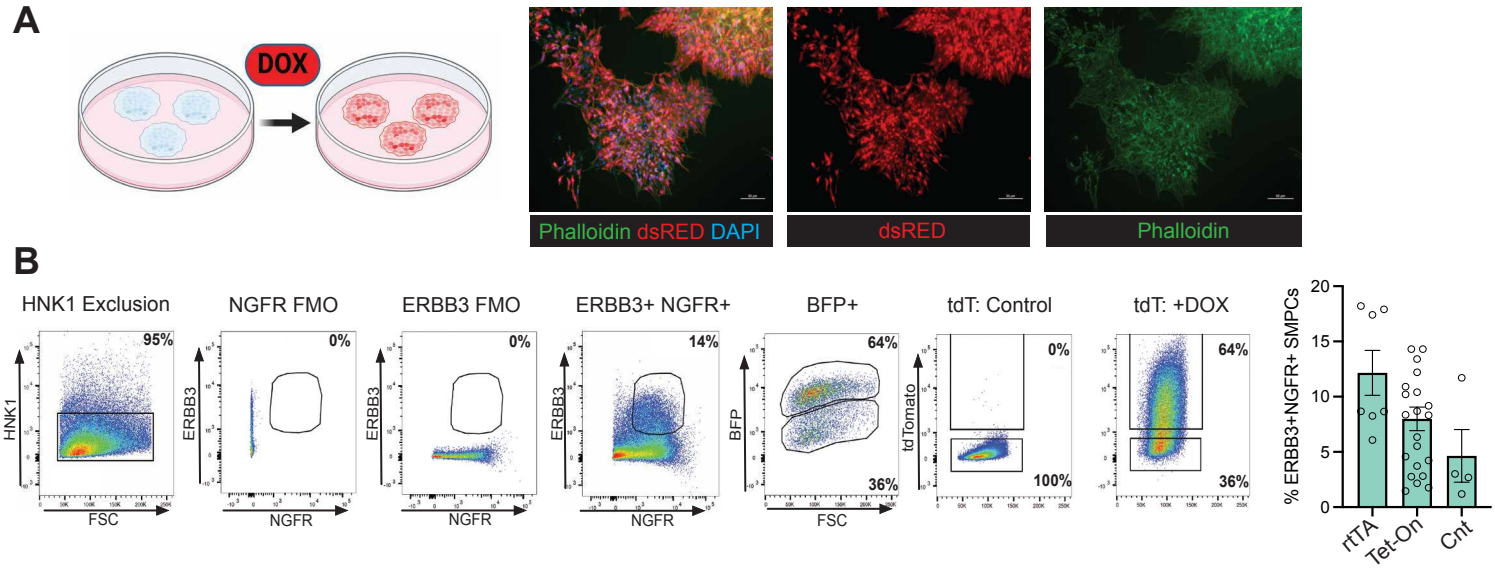

A
SMPC changes across time
ACVR1
BMP1
ADAMTS16
PDLIM7
FGFR4
LAMTOR2
ABLIM3
CASZ1
NEO1
LRRC27
BMPR2
CCNG2
CDK6
SERPINE1
LYRM2
LRRN1
D1 D5 D10
Z-score
Time
Day 1
Day 5
Day 10
Day 20
NOTCH3
ACVR1
LRRN1
CDK6
B
Myocyte changes across time
DLL1
NOTCH1
MEGF10
DAG1
LAMA5
SIK1
CARMIL3
EMILIN2
MYMK
JAM2
ERBB2
CAV3
ACHE
MYOM3
GATA2
MEGF8
PRDM12
ISL2
D1 D5 D10 D20
MEGF10
DLL1
MYOM3
MCAM
C
PCA of Myofiber Heterogeneity
PC2: 17% variance
PC1: 23% variance
Time
Day 5
Day 10
Day 20
Myofiber Type
Hm-only
Chimeric
Chimeric
204 genes
Human-only
498 genes
-LOG10padj
LOG2FoldChange
MYH1
MYH2
CKM
ALDOA
FHL1
MYH4
LRRN1
PEG10
MYOG
DLK1
MYL4
ACTC1
MYH3
CHRND
D
Hm-only myofiber changes across time
THBS4
THBS1
LRRN1
SP7
SPTAN1
LYRM2
FN1
COL1A2
MEGF8
ITGA6
CDK15
MPZ
MYL3
DMD
CXCL14
ATF5
CHRNA10
MYOM1
NPM3
D10 D20
Z-score
THBS4
MYH4
Hm-only Chimeric
Time
Day5
Day10
Day20
E
Chimeric myofiber changes across time
CHAT
MYH8
PAM16
MYOM2
TGFB3
TPM1
COL5A3
LDHB
THBS4
MYH4
COL1A2
FGF14
ADAMTS2
ALG2
COL1A1
LAMA4
D5 D10 D20
Z-score
ACTC1
VEGFA
Hm-only Chimeric
Hm only Chimeric
Time
Day5
Day10
Day20

A

Mouse Model	ROIs Collected			Total
	PAX7+ SMPC	Human-Only Myofiber	Chimeric Myofiber	
WildType Pre	13	15	0	70
WildType Post	13	18	5	41
MDX Pre	6	9	11	20
MDX Post	8	12	15	32

B

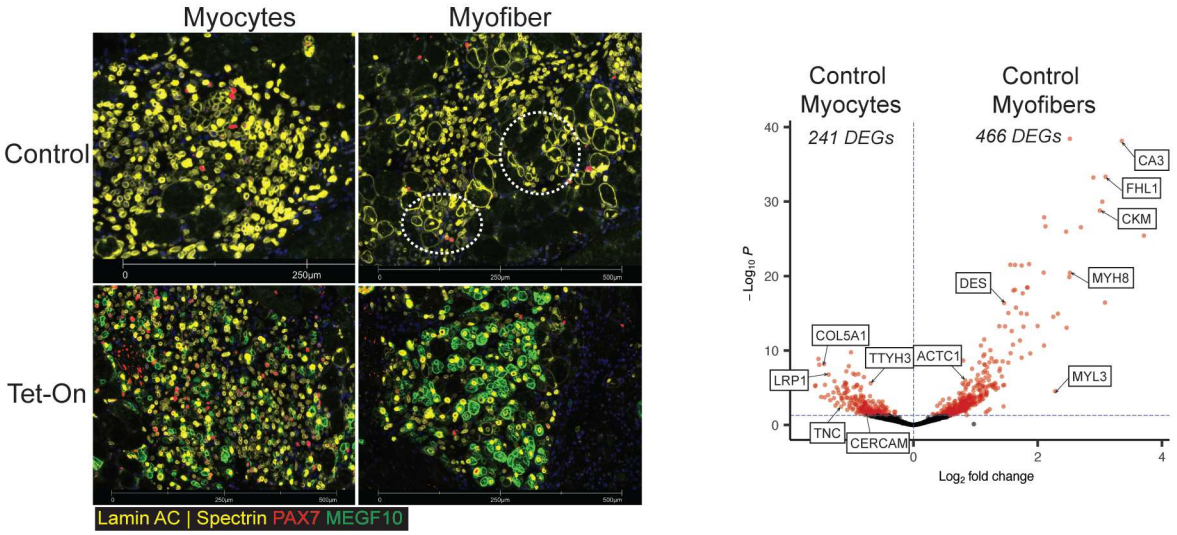



A
DOX
Phalloidin dsRED DAPI
dsRED
Phalloidin
B
HNK1 Exclusion
NGFR FMO
ERBB3 FMO
ERBB3+ NGFR+
BFP+
tdT: Control
tdT: +DOX
95%
0%
0%
14%
64%
0%
100%
64%
36%
HNK1
ERBB3
BFP
tdTomato
FSC
NGFR
% ERBB3+NGFR+ SMPCs
rtTA
Tet-On
Cnt
C
Control
2 µg/mL DOX
0%
42%
tdT
FSC-A
****
% tdT+ SMPCs
Control
1µg/mL
2µg/mL
5µg/mL
10µg/mL
20µg/mL
Doxycycline
D
Control
EMARDD-Tak
EMARDD-Logan
ERBB3-PECy7
NGFR-APC
% ERBB3+NGFR+ SMPCs
Cnt.
Logan
Tak.

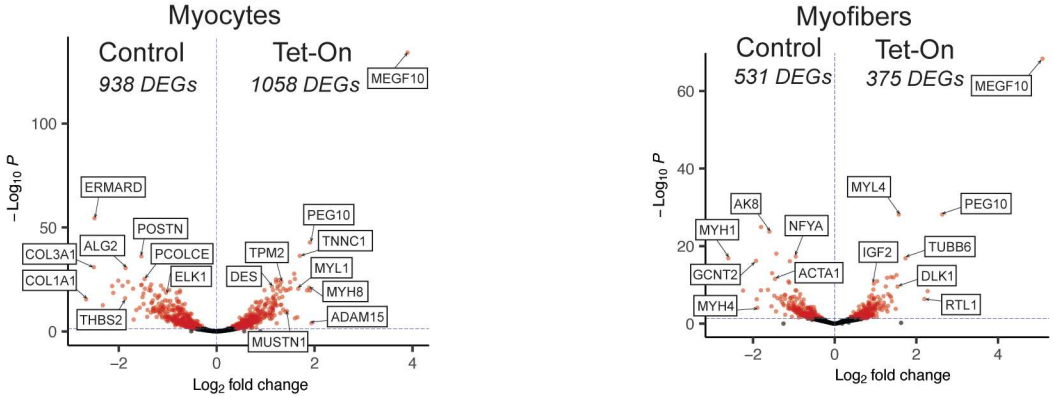
A

Condition	ROIs Collected				Total
	PAX7+ SMPC	Myocyte	Human-only Myofiber	Chimeric Myofiber	
Control Day 10	14	14	8	7	43
Tet-On Day 10	22	13	17	0	42

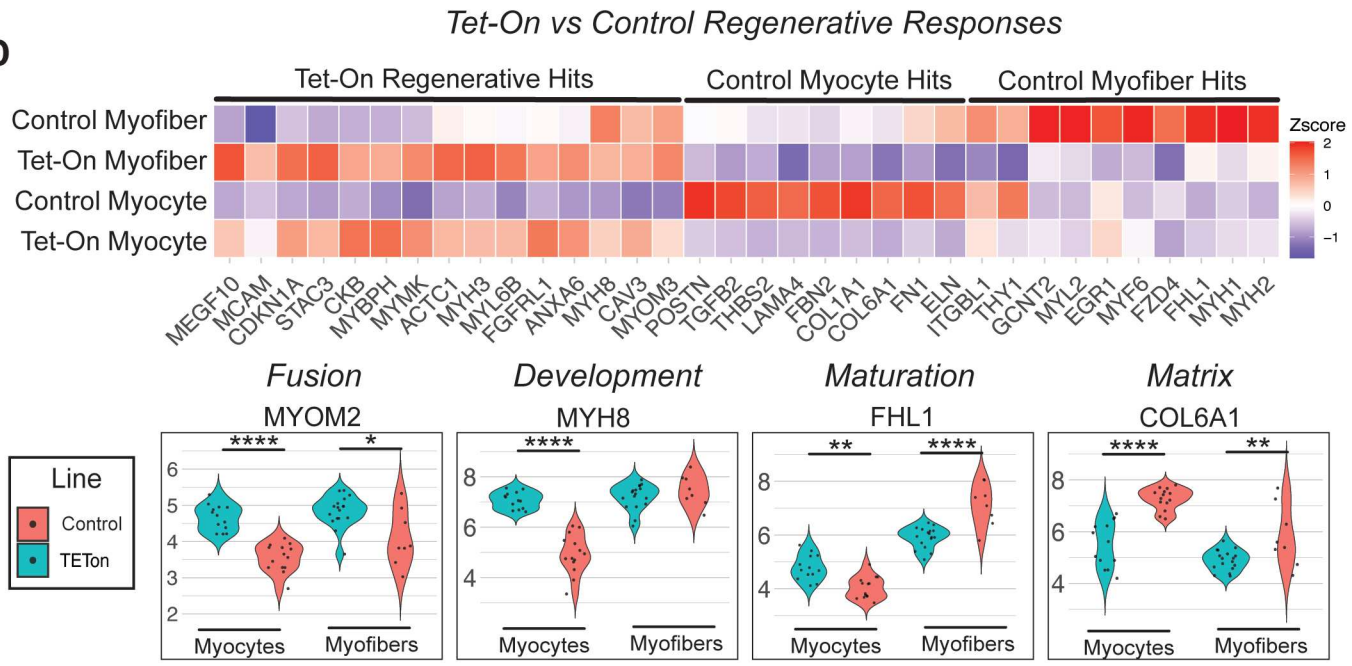
B



C



D



Supplementary Files

This is a list of supplementary files associated with this preprint. Click to download.

- EXTENDEDMETHODS.pdf
- TableS1.xlsx
- TableS2.xlsx
- TableS3.xlsx
- TableS4.xlsx